JOURNAL OF GEOPHYSICAL RESEARCH: SOLID EARTH, VOL. 118, 1240–1267, doi:10.1002/jgrb.50116, 2013

Source parameter inversion for recent great earthquakes from a decade-long observation of global gravity fields

Shin-Chan Han,[1] Riccardo Riva,[2] Jeanne Sauber,[1] and Emile Okal[3]

Received 4 September 2012; revised 31 January 2013; accepted 1 February 2013; published 26 March 2013.

[1] We quantify gravity changes after great earthquakes present within the 10 year long time series of monthly Gravity Recovery and Climate Experiment (GRACE) gravity fields. Using spherical harmonic normal-mode formulation, the respective source parameters of moment tensor and double-couple were estimated. For the 2004 Sumatra-Andaman earthquake, the gravity data indicate a composite moment of 1.2×10^{23} N m with a dip of 10°, in agreement with the estimate obtained at ultralong seismic periods. For the 2010 Maule earthquake, the GRACE solutions range from 2.0 to 2.7×10^{22} N m for dips of 12°–24° and centroid depths within the lower crust. For the 2011 Tohoku-Oki earthquake, the estimated scalar moments range from 4.1 to 6.1×10^{22} N m, with dips of 9°–19° and centroid depths within the lower crust. For the 2012 Indian Ocean strike-slip earthquakes, the gravity data delineate a composite moment of 1.9×10^{22} N m regardless of the centroid depth, comparing favorably with the total moment of the main ruptures and aftershocks. The smallest event we successfully analyzed with GRACE was the 2007 Bengkulu earthquake with $M_0 \sim 5.0 \times 10^{21}$ N m. We found that the gravity data constrain the focal mechanism with the centroid only within the upper and lower crustal layers for thrust events. Deeper sources (i.e., in the upper mantle) could not reproduce the gravity observation as the larger rigidity and bulk modulus at mantle depths inhibit the interior from changing its volume, thus reducing the negative gravity component. Focal mechanisms and seismic moments obtained in this study represent the behavior of the sources on temporal and spatial scales exceeding the seismic and geodetic spectrum.

Citation: Han, S.-C., R. Riva, J. Sauber, and E. Okal (2013), Source parameter inversion for recent great earthquakes from a decade-long observation of global gravity fields, *J. Geophys. Res. Solid Earth*, *118*, 1240–1267, doi:10.1002/jgrb.50116.

1. Introduction

[2] Large-scale processes of geophysical and climate-related mass redistribution cause changes in the gravitational potential field. By observing the relative motions of two identical satellites (orbiting proof masses), the Gravity Recovery and Climate Experiment (GRACE) mission has been mapping the spatial distribution of surface and interior mass flux and transport as well as adjustments in the Earth system since its launch in 2002 [*Tapley et al*., 2005]. As one of such processes, earthquakes cause variations in the gravitational potential field at a spatial scale up to some thousands of kilometers and at temporal scales of seconds to decades, by radiating seismic energy and deforming the surface and interior permanently and gradually.

[3] Traditional coseismic and postseismic observations have measured surface displacements such as ground, seafloor, and sea-surface motions using a variety of instruments: seismometers, strainmeters, leveling, GPS, Interferometric Synthetic Aperture Radar (InSAR), seafloor transponders, and tsunami gauges. These have been the primary tools used to understand the rupture dynamics, the spatial extent of slip, and gradual postseismic changes. However, space-borne gravimetric observations are also sensitive, in particular, to interior deformation in the broader region affected by the rupture, including the oceanic environment largely inaccessible by traditional measurements. Specifically, they could fill in the seldom-observed long wavelength spectrum of earthquake observations as a complement to surface geodetic measurements and seismic data. In addition, they reflect an average deformation over a time window much longer than that accessible from seismic data which is limited in principle by the period of the Earth's gravest mode, ${}_0S_2$ (3232 s). We examine this new type of earthquake observations from GRACE gravimetry, which are sensitive to changes in gravitational potential which we express in the formalism of the Earth's normal modes, as an alternative to the study of vertical and horizontal displacements, in order to seek additional information on earthquake mechanisms and a new perspective on earthquake-related processes.

[1]Planetary Geodynamics Laboratory, NASA Goddard Space Flight Center, Greenbelt, Maryland, USA.
[2]Department of Geoscience and Remote Sensing, Delft University of Technology, Delft, Netherlands.
[3]Department of Earth and Planetary Sciences, Northwestern University, Evanston, Illinois, USA.

Corresponding author: S.-C. Han, Planetary Geodynamics Laboratory, NASA Goddard Space Flight Center, Greenbelt, MD, USA (shin-chan.han@nasa.gov)

2169-9313/13/10.1002/jgrb.50116

[4] We scrutinize the observations of global gravitational potential change after the following recent megathrust earthquakes: 2004 Sumatra-Andaman ($M_w = 9.15$ to 9.3), characterized by a slip greater than 3 m over more than 1200 km of fault length [e.g., *Tsai et al*., 2005; *Chlieh et al*., 2007]; 2007 Bengkulu (Sumatra; $M_w = 8.5$) [e.g., *Borrero et al*., 2009]; 2010 Maule, Chile ($M_w = 8.8$) with slip greater than 3 m over 450 km [e.g., *Pollitz*, *et al*., 2011]; and 2011 Tohoku-Oki ($M_w \approx 9.0$) with slip greater than 5 m over 330 km [e.g., *Simons et al*., 2011]. In addition to these thrust sources, and for the first time, we analyze gravitational perturbations due to the sequence of great strike-slip earthquakes (cumulative $M_w \approx 8.7$) which ruptured in 2012 100–200 km southwest of the Sumatra subduction zone [e.g., *Yue et al*., 2012].

[5] Such gravity changes are caused dominantly by large-scale density change in the region surrounding the rupture and by surface deformation, including interaction with the ocean, as suggested by *Han et al*. [2006] and others thereafter. The surface deformation, however, would be expected to be small in large-scale gravity change for vertical strike-slip earthquakes. Sea level changes due to coseismic gravitational potential changes have been addressed more recently by *de Linage et al*. [2009], *Broerse et al*. [2011], and *Cambiotti et al*. [2011]. While most of these analyses, including *Heki and Matsuo* [2010], *Matsuo and Heki* [2011], and *Wang et al*. [2012], used the monthly time series of GRACE gravity maps, *Han et al*. [2010, 2011] also directly exploited the fundamental observations of range-rate change after earthquakes to optimize spatial and temporal resolution. *Han et al*. [2011] and *Cambiotti et al*. [2012] inverted the GRACE range-rate and monthly gravity data, respectively, to quantify the fault parameters of the 2011 Tohoku-Oki earthquake. Various numerical modeling approaches from a half-space [*Okubo*, 1992] to a layered spherical Earth model [*Pollitz*, 1996], considering the ocean layer and sea level feedback [*Broerse et al*., 2011; *Cambiotti et al*., 2011], have been used to compute synthetic gravity changes. Furthermore, the postseismic gravity change after the 2004 Sumatra-Andaman rupture was also identified and such observations were interpreted considering the Earth's rheological response to mega-earthquakes [*Han et al*., 2008; *Panet et al*., 2010; *Hoechner et al*., 2011] and the diffusion of water in the mantle [*Ogawa and Heki*, 2007].

[6] In this study, we present a theoretical model of the coseismic gravitational potential for a spherical Earth on the basis of gravitational potential normal mode summation, as also envisaged by *Chao and Gross* [1987] and *de Linage et al*. [2009]. We particularly examine the gravitational characteristics of normal modes as a function of the Earth's elastic structure and the earthquake source depth. We evaluate and discuss the effects of surficial layering (including the ocean) and density change on the gravity change. Next, we formulate inverse models to estimate the moment tensor components and subsequently fault parameters from the GRACE data for each earthquake. We use the readily available level 2 (L2) data products from the GRACE mission that implies monthly snapshots of global gravitational potential changes with a spatial resolution of 400–500 km. Finally, we apply this inversion approach to characterize these earthquakes with (point) centroid source representation; discuss the fault solution estimates of moment, dip, strike, rake and depth, and the trade-offs among these parameters; and compare these great earthquakes based on homogeneous data, consistent gravity modeling, and uniform inversion methodology. Although the gradual postseismic changes after the rupture were also evident in the data, this study is focused on the coseismic change in the gravitational potential and leaves out the longer-term postseismic response to a future investigation.

2. Coseismic Gravitational Potential Change Due to a Double-Couple Source

[7] We derive the expression of coseismic changes in gravitational potential due to a point dislocation on the basis of gravitational potential normal mode summation. Our goal is to obtain the representation in terms of spherical harmonic coefficients for the coseismic gravitational potential changes as explicit functions of the parameters of a point-source double-couple (scalar seismic moment M_0, dip δ, rake λ, and strike ϕ_f). In the end, we will use these results to analyze global gravity data such as from GRACE to invert earthquake source processes.

[8] The concept that gravity participates in the restoring force controlling the oscillation of a deformed elastic Earth was first expressed by *Bromwich* [1898], following *Lamb*'s [1882] estimate of its period of free oscillation. Ever since *Love*'s [1911] classical study, which provided the first theoretical computation of the fundamental mode of a compressible, elastic gravitating Earth, all detailed computations of the Earth's normal modes [e.g., *Pekeris and Jarosch*, 1958; *Gilbert and Backus*, 1968] have included the relevant variations of its gravitational potential. Because they do not result in changes in its gravity field, the torsional modes of oscillation of the Earth will be ignored from the rest of this paper.

[9] The problem of the excitation of a normal mode by a seismic source was first described by *Alterman et al*. [1959] and given a simple and elegant formulation by *Gilbert* [1970]. This set the stage for the use of normal mode summation to synthesize either seismic waves, which express the transient deformation following an earthquake [e.g., *Kanamori and Cipar*, 1974] or geodetic displacements, which express permanent coseismic deformation [*Pollitz*, 1996]. Thus, it should be possible to similarly describe any static or transient changes in the Earth's gravitational potential on the basis of a summation of its normal modes. Indeed, this approach goes back to *Longman* [1962, 1963] in the simpler case of the loading of the Earth by a point mass.

[10] In the notation of *Kanamori and Cipar* [1974, Figure 10] and *Kanamori and Given* [1981, Figure 1], we recall that the radial displacement u_r (as would be recorded by a vertical seismometer), excited by a point-source double-couple can be expanded as

$$\begin{aligned} u_r(r,\theta,\phi;t) = M_0 \cdot \sum_{n,l} y_1(r)[-s_R K_0 P_{l,0}(\cos\theta) + q_R K_1 P_{l,1}(\cos\theta) \\ - p_R K_2 P_{l,2}(\cos\theta)] \\ \times [1 - \cos({}_n\omega_l t) \cdot \exp(-{}_n\omega_l t / 2\,{}_nQ_l)]. \end{aligned} \tag{1}$$

[11] The definition of the associated Legendre functions $P_{l,m}$ used here is such that they are normalized to a constant integral of 4π on the sphere, which relates them to the Legendre functions P_l^m used, for example, by *Kanamori and Cipar* [1974] through

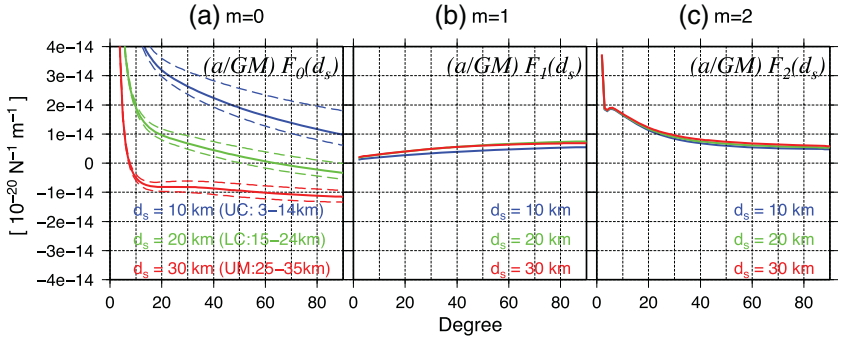

Figure 1. Spectrum of the three gravitational excitation functions evaluated at depths $d_s = 10$, 20, and 30 km; (a) $F_0(d_s) = \sum_n K_0(d_s) y_5(a)$ (isotropic, $m = 0$), (b) $F_1(d_s) = \sum_n K_1(d_s) y_5(a)$ (dipolar, $m = 1$), and (c) $F_2(d_s) = \sum_n K_2(d_s) y_5(a)$ (quadrupolar, $m = 2$). For Figure 1a, the isotropic function is also evaluated at the upper and lower bounds of each distinct layer in PREM (i.e., upper crust, lower crust, and upper mantle) and shown as dashed lines.

$$P_{l,m} = \sqrt{k(2l+1)\frac{(l-m)!}{(l+m)!}} \cdot P_l^m, \tag{2}$$

where $k = 1$ is for $m = 0$ and $k = 2$ otherwise. The expansion in equation (1) uses a system of spherical harmonics whose pole is chosen at the seismic epicenter, and whose primary meridian is taken along the dislocation fault strike. Under this geometry, a point-source double-couple excites only the modes of azimuthal orders $m = 0, \pm 1$, and ± 2, allowing the expansion (1) to contain only three terms inside the first bracket; s_R, q_R, and p_R are then trigonometric parameters depending only on the geometry of the dislocation (dip angle δ and rake λ), and on the longitude ϕ of the receiver, measured from the fault strike [*Kanamori and Cipar*, 1974, Figure 10]:

$$\begin{aligned} sR &= \sin\lambda \sin\delta \cos\delta, \\ q_R &= \sin\lambda \cos 2\delta \sin\phi + \cos\lambda \cos\delta \cos\phi, \\ p_R &= \cos\lambda \sin\delta \sin 2\phi - \sin\lambda \sin\delta \cos\delta \cos 2\phi, \\ \phi &= \phi_f - \phi_r = \phi_{lon} + \phi_f - \pi, \end{aligned} \tag{3}$$

where ϕ_f is the azimuth of the fault strike, and ϕ_r the azimuth of the small arc of great circle departing the source to the receiver, both measured clockwise from local north at the epicenter (alternatively, $\phi_r = \pi - \phi_{lon}$, where ϕ_{lon} would be the longitude of the receiver in a frame where the pole is at the epicenter, measured counterclockwise from the direction of local south at the source). y_1 is the vertical displacement component of the eigenfunction (dependent on degree l and overtone number n) [*Alterman et al.*, 1959; *Saito*, 1967]. The functions K_0, K_1, and K_2, of which explicit forms are given in *Kanamori and Cipar* [1974], describe the excitation of a full Earth oscillation by a seismic source, as such depends only on l and n as well as on the specific Earth model used, and of course on the depth d_s of the source, but no longer on the particular orientation of either the source or the receiver. The temporal part expressed as the second bracket of equation (1) consists of a static term describing the permanent deformation of the Earth (expressed as the "1" in the bracket) and of a transient oscillatory term "seismic waves" corresponding to the attenuated sinusoid. An equivalent expression using moment tensor components can be found in *Kanamori and Given* [1981] and *Pollitz* [1996].

[12] This formalism can be extended immediately to the case of the variations in gravitational potential $\psi(r,\theta,\phi_{lon})$ by replacing the first component y_1 of the eigenfunction by the fifth one, y_5, as introduced by *Alterman et al.* [1959]. In the particular case of the permanent "static" variation of the potential at the Earth's surface ($r = a$), one simply obtains

$$\begin{aligned} \psi(\theta, \phi_{lon}) = M_0 \cdot \sum_{n,l} y_5(a) \cdot [& -s_R K_0 P_{l,0}(\cos\theta) \\ & + q_R K_1 P_{l,1}(\cos\theta) - p_R K_2 P_{l,2}(\cos\theta)]. \end{aligned} \tag{4}$$

[13] Note that y_5 is computed routinely as part of the solution of the full elastogravitational eigenproblem of the free oscillation and that its inclusion is particularly critical to the accurate determination of the period of the gravest modes, in particular, the radial ones ($l = 0$). However, the information contained in y_5 has rarely been used, since most applications of normal mode theory have been limited to seismology, before the advent of detailed large-scale gravity observations, notably with programs such as GRACE [*Tapley et al.*, 2005].

[14] By substituting equation (3), equation (4) can be rewritten as follows:

$$\psi(\theta, \phi_{lon}) = \frac{GM}{a} \sum_l \sum_{m=0}^{2} P_{l,m}(\cos\theta) \{ C_{l,m} \cos m\phi_{lon} + S_{l,m} \sin m\phi_{lon} \}, \tag{5}$$

where G is the universal gravitational constant, M the mass of the Earth, and a its radius. The five non-trivial dimensionless coefficients are defined, with the moment tensor components following the convention by *Aki and Richards* [1980] as follows:

$$C_{l,0} = \frac{a}{GM} \left[\sum_n K_0(d_s) y_5(a) \right] \cdot \left(\frac{-M_{rr}}{2} \right), \tag{6a}$$

$$C_{l,1} = \frac{a}{GM} \left[\sum_n K_1(d_s) y_5(a) \right] \cdot (M_{r\theta}), \tag{6b}$$

$$S_{l,1} = \frac{a}{GM} \left[\sum_n K_1(d_s) y_5(a) \right] \cdot (M_{r\phi}), \tag{6c}$$

$$C_{l,2} = \frac{a}{GM} \left[\sum_n K_2(d_s) y_5(a) \right] \cdot \left(\frac{M_{\theta\theta} - M_{\phi\phi}}{2} \right), \tag{6d}$$

$$S_{l,2} = \frac{a}{GM}\left[\sum_n K_2(d_s)y_5(a)\right]\cdot\left(M_{\theta\phi}\right), \tag{6e}$$

where $M_{rr} = M_0 \sin 2\delta \sin\lambda$,

$$M_{r\theta} = -M_0\left(\cos\delta\cos\lambda\cos\phi_f + \cos 2\delta \sin\lambda \sin\phi_f\right),$$
$$M_{r\phi} = -M_0\left(-\cos\delta\cos\lambda\sin\phi_f + \cos 2\delta \sin\lambda\cos\phi_f\right),$$
$$M_{\theta\theta} - M_{\phi\phi} = -M_0\left(2\sin\delta\cos\lambda\cdot\sin 2\phi_f - \sin 2\delta\sin\lambda\cdot\cos 2\phi_f\right), \text{ and}$$
$$M_{\theta\phi} = -M_0\left(\frac{1}{2}\sin 2\delta\sin\lambda\sin 2\phi_f + \sin\delta\cos\lambda\cos 2\phi_f\right).$$

[15] In equation (6) and for each value of degree l, the summations in the functions $F_m = \sum_n K_m(d_s)y_5(a)$, $(m = 0, 1, 2)$ are performed over the overtone number n on which the individual values of $y_5(a)$ and the $K_m(d_s)$ will of course depend. In particular, these functions of l are now characteristic of the (laterally homogeneous) Earth model, but no longer depend on any property of the seismic source (excluding depth through the $K_m(d_s)$), and as such, they can be precomputed for any combination of l and d_s.

[16] These functions are closely related to the coefficients $y_1^{lm(S)}$ used to expand radial deformation by *Pollitz* [1996, equation (3a)], except that we express them with sines and cosines as opposed to imaginary exponentials and that *Pollitz* [1996] considered only elastic (and not gravitational) restoring forces. *Pollitz* [1992] showed in considerable detail (including the effect of gravity) that it is possible to compute directly the functions F_m from the equations of equilibrium of the deformed Earth, rather than explicitly summing over an a priori infinite number of overtones n, as in equation (6). We follow here an approach similar to *Piersanti et al.*'s [1995] and *Pollitz et al.*'s [2006] studies, which consists of casting the static problem of the equilibrium of a layered gravitating elastic Earth in the same formalism as the dynamic one for a free oscillation, but of course in the absence of any time-dependent terms, following in the footsteps of *Longman* [1963] and *Smylie and Mansinha* [1971].

[17] In this framework and given a point-source double-couple of prescribed geometry and amplitude (M_0), imbedded at the depth d_s in an elastic Earth, *Pollitz*' [1996] formalism consists of expanding its field of discontinuities (obtained under a representation theorem) onto spherical harmonics, and of defining, for each degree l and orders $m = 0$, 1, and 2, an equivalent discontinuity at the depth d_s in the four components of the eigenvector $\mathbf{y}$ of the static problem (which remains independent of m). In the presence of gravity, we generalize it by imposing the continuity of the additional components, y_5 and y_6, for $r = r_s$ ($r_s = a - d_s$), thus imposing six boundary conditions on the full six-dimensional elastogravitational eigenvector $\mathbf{y}$. Following *Pollitz et al.* [2006] and because $\mathbf{y}$ is continuous at all depths $d \neq d_s$, except at the core-mantle boundary as discussed for example by *Smylie and Mansinha* [1971], it can be integrated continuously upwards to $r = r_s^-$ from the core-mantle boundary, where initial conditions feature three degrees of freedom, detailed for example by *Vermeersen et al.* [1996], in the framework of *Chinnery*'s [1975] explanation of the so-called Longman's paradox. Similarly, it can be integrated from the surface of the Earth (where there are again three degrees of freedom) downwards to r_s^+. For each $m = 0$, 1, and 2, the six boundary conditions at $r = r_s$ define the proper combination of initial conditions from which the value of $y_5(a)$ can be computed and equated to F_m.

[18] As mentioned above, equations in (6) are relatively simple because they are written in a particular system of spherical harmonics, where the pole is at the seismic epicenter and the prime meridian oriented along the local south, since under this geometry, a point-source double-couple excites only azimuthal orders $m = 0$, $\pm$ 1, and $\pm$ 2. That frame will hereafter be identified with a superscript s. However, when studying the gravity field of the Earth, the convention is to use the geographic spherical harmonics, defined about its axis of rotation (the North Pole) and the prime Greenwich meridian, hereafter be identified with a superscript g. Therefore, one has to project one system of spherical harmonics onto the other, in order to express equation (6) in the geographic harmonics; this relatively classical problem [e.g., *Sato*, 1950; *Brink and Satchler*, 1968; *Stein and Geller*, 1977] is carried out as a succession of two solid rotations: The first one (of amplitude θ_s, the colatitude of the epicenter) is taken about the pole of the geographic meridian going through the epicenter and brings back the pole of the spherical harmonics to the geographic North Pole, and the second one (of amplitude $-\phi_s$, the opposite of the longitude of the epicenter) is taken about the axis of rotation of the Earth and restores the Greenwich meridian as the primary one.

[19] Regrouping the coefficients $C_{l,i}$ and $S_{l,i}$ in equation (6) in the form of a vector $\mathbf{X}_l^s$ ($X^s_{l,-2} = S_{l,2}$, $X^s_{l,-1} = S_{l,1}$, $X^s_{l,0} = C_{l,0}$, $X^s_{l,1} = C_{l,1}$, and $X^s_{l,2} = C_{l,2}$), the projection onto the geographic harmonics is expressed as a new vector $\mathbf{X}_l^g$:

$$X^g_{l,m}\left(M_0, \phi_f\delta, \lambda, d_s, \theta_s, \phi_s\right) = \sum_{\substack{i=-2 \\ -l\le m\le l,}}^{2} E^l_{m,i}(\theta_s, \phi_s)X^s_{l,i}\left(M_0, \phi_f\delta, \lambda, d_s\right) \tag{7}$$

where the factor E expresses the combination of two rotations. Note that despite its apparent complexity, equation (7) remains a completely linear operation on the various components of the vector $\mathbf{X}_l^s$.

[20] A fundamental aspect of equation (7) is that while the potential field resulting from a dislocation expressed as a point-source double-couple could be expanded on harmonics of orders $m = 0$, $\pm$ 1, and $\pm$ 2 in the source-based system ($\mathbf{X}_l^s$ being five-dimensional), it will project on all orders ($-l \le m \le l$) in the geographic system centered at the North Pole ($\mathbf{X}_l^g$ being $(2l+1)$-dimensional). Note that a similar approach is used when studying the splitting of the free oscillations of the Earth due to rotation and ellipticity, with the identical result that normal modes excited by an earthquake are split into all of their $(2l+1)$ singlets ($-l \le m \le l$) [*Stein and Geller*, 1977].

3. Coseismic Gravitational Response Functions

[21] We characterize the coseismic changes in gravitational potential ψ through the functions

$$F_m(d_s) = \sum_n K_m(d_s)y_5(a), \tag{8}$$

with orders $m = 0$, 1, 2 for isotropic, dipolar, and quadrupolar excitations, respectively. They represent the Earth's gravimetric response to faulting by a double-couple and depend

only on Earth structure, degree l, and source depth d_s. Figure 1 presents examples of these functions, computed for the Preliminary Reference Earth Model (PREM) model [*Dziewonski and Anderson*, 1981] at three representative depths (10, 20, and 30 km), sampling the upper crustal (3–15 km), lower crustal (15–24 km), and upper mantle (24–80 km) layers of the model.

[22] As shown in Figure 1, the behavior with l of the three functions is significantly different. Both F_1 and F_2 are weakly dependent on depth and monotonic (respectively, increasing and decreasing functions of l) functions, while F_0 strongly depends on depth, to the extent that it even reverses sign, with the nodal degree decreasing with increasing depth. This strong dependence of F_0 on depth is further investigated by computing its values at the upper and lower bounds of each source layer, shown as dashed lines on Figure 1a; they suggest a moderate dependence of F_0 with depth within a layer, but a significant one between layers, which illustrates the critical dependence of the coefficients K_0 on the elastic moduli at the source. The spatial pattern of F_m at different depths is shown in Figure 2, truncated at degree 50 (i.e., spatial resolution of 400 km). The isotropic term, F_0, is dominant when the source is at the lower depth, while the non-isotropics, F_1 and F_2, become more pronounced as the source depth increases.

[23] Several features of Figures 1 and 2 are straightforward to interpret in the context of classical results of normal mode seismology. In particular, we recall that the strike-slip coefficient K_2 is proportional to y_3/r_s. In the vicinity of the Earth's surface, where the shear stress y_4 vanishes, the logarithmic derivative of this quantity takes the value $\frac{r}{y_3}\cdot\frac{d}{dr}\left(\frac{y_3}{r}\right) = -\frac{1}{r}\frac{y_1}{y_3} \approx -\frac{l}{a}\frac{u_z}{u_x}$, on the order of $-l/a$ for $l > 1$, and for branches of modes featuring a reasonably circular ground motion at the surface (e.g., fundamental Rayleigh waves for which this ratio approaches 1.5). Thus, the characteristic depth for the decay of K_2 near the surface is on the order of a/l, which means that K_2 is essentially independent of depth for shallow earthquakes, a well-known property of mantle Rayleigh waves. This explains the lack of dependence of F_2 on depth, as exhibited in Figure 1c. By contrast, the coefficient K_1, proportional to y_4/μ, vanishes at the surface, leading to the classical singularity in excitation by dip-slip components at shallow depths [e.g., *Kanamori and Given*, 1981]. For shallow sources (d_s much less than one wavelength), y_4 is expected to be continuous and grow linearly with depth; however, μ will suffer discontinuities in the various layers of the Earth, leading to a much slower growth (or even an irregular behavior) of K_1 with depth. As for the isotropic coefficient K_0, involved (together with K_2) in the case of a dipping (e.g., thrust) fault, its more complex expression as a function of the eigenvector $\mathbf{y}$ precludes any simple interpretation of its variation with depth.

[24] The physical origin of the change in gravitational potential at the surface, $y_5(a)$, can be separated into two contributions, namely (i) a displacement of the free boundary of the Earth, resulting in the filling of an initially void volume by material of finite density and (ii) the effect on ψ at the surface of changes in density within the interior of the planet, resulting from its deformation, including that of surfaces of

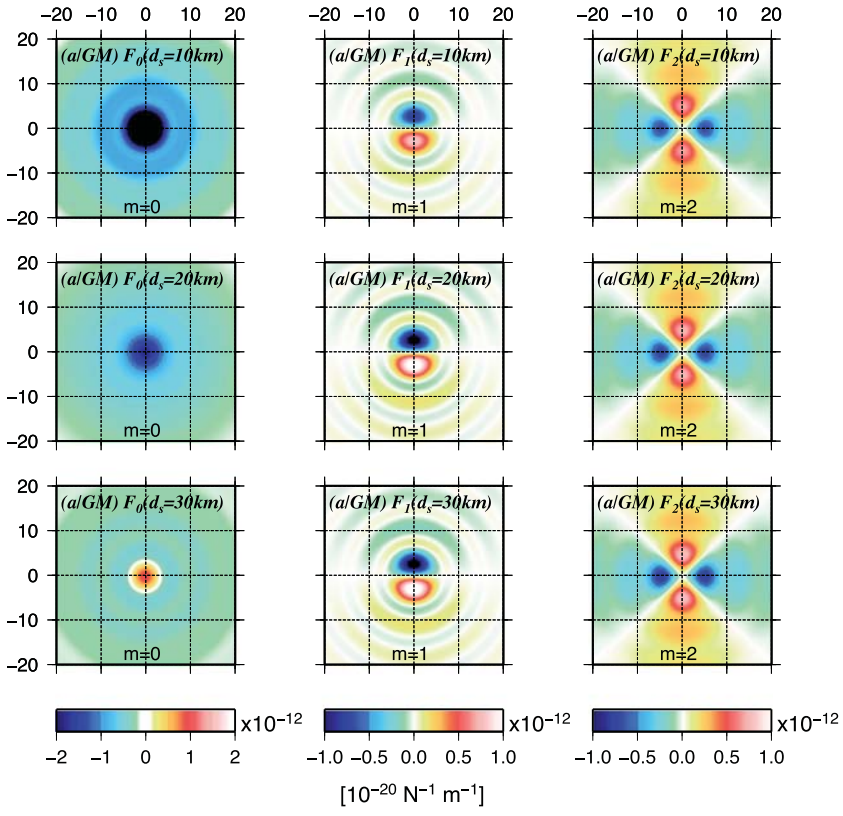

Figure 2. Spatial patterns of the functions $F_m(d_s)$ in the vicinity of the source, evaluated at depths of 10, 20, and 30 km.

discontinuity, such as the crust-mantle interface. For (ii), the gravitational effect of the (coseismic) change of discontinuity in interior density stratification is considerably smaller than the interior density change by compression and/or dilatation [*Pollitz*, 1997; *Han et al*., 2006]. In the limit of large-scale gravity changes (a few 100 km), the effect from (ii) is as large as (i), while (i) overwhelms (ii) at much smaller scales, as shown in *Han et al*. [2006].

[25] The change in gravitational potential due to the deformation of the surface, $F_m^{(B)}$, is in the nature of a Bouguer effect, and can be easily computed from the radial displacement component of the eigenvector, $y_1(a)$. In the limit $y_1 < a/l$ (i.e., the vertical deformation being smaller than its lateral dimension), the contributing material can be modeled as a thin layer of thickness y_1 and density $\Delta\rho$ (crustal density for inland earthquakes, reduced by seawater density for undersea ones), leading the classical result [*Jeffreys*, 1976; *Turcotte et al*., 1981]:

$$F_m^{(B)} = \sum_n K_m(d_s)\frac{4\pi G a \Delta\rho}{(2l+1)} y_1(a), \quad m = 0, 1, 2. \tag{9}$$

[26] The degree-dependent scale factor multiplying the y_1 eigenfunction is needed to convert the thin layer mass anomaly $\Delta\rho y_1(a)$ into the gravitational potential anomaly at the surface. The contribution from the interior deformation (mostly due to coseismic dilatation or compression of the material surrounding the source) is computed by removing this superficial (or Bouguer) contribution from the full variation F_m as

$$F_m^{(I)} = F_m - F_m^{(B)} = \sum_n K_m(d_s)\left(y_5(a) - \frac{4\pi G a \Delta\rho}{(2l+1)} y_1(a)\right), \quad m = 0, 1, 2. \tag{10}$$

[27] Although we did include self-gravitation and loading when computing the functions F_m and for the sake of simplicity, they are not discussed here, as their contributions are considerably smaller than the simple Bouguer effect expressed by equation (10); see *de Linage et al*. [2009] and *Cambiotti et al*. [2011] for details. The degree-dependent behaviors of equations (9) and (10) at three different depths are shown in Figure 3, where the sign for the surface deformation function for $m = 0$ was reversed in the plot. As for the case of total gravity change in Figure 1, the depth-dependence is found to be significant in the isotropic case, where the interior deformation shows even greater depth-dependence. For the isotropic component, which is directly related to dilatation at the source (see Appendix A), the interior deformation $F_0^{(I)}$, $(m = 0)$ contributes more signal than the Bouguer term $F_0^{(B)}$ when the source locates at shallower depth (10 km, within the upper crust) where the material is more compressible. In contrast, $F_0^{(B)}$ becomes prominent when the source is deeper (i.e., 30 km, within the upper mantle) where the material is less compressible. In the dipolar case ($m = 1$), the change in potential is largely due to the Bouguer term $F_1^{(B)}$ at all depths, while in the quadrupolar case ($m = 2$), $F_2^{(I)}$ remains prominent at all depths.

[28] We computed the coseismic potential change from a synthetic double-couple at different depths (using a compressible Earth model with an ocean layer). A centroid with a scalar moment $M_0 = 5.0 \times 10^{22}$ N m ($M_w = 9.0$) and strike $\phi_f = 180°$, dip $\delta = 15°$, and rake $\lambda = 90°$ was used. The gravity changes (up to degree and order 40, or equivalently a spatial resolution of 500 km) from the same seismic source but at different depths are compared in Figure 4. The effect of the isotropic term ($m = 0$), mostly responsible for a large central negative anomaly, decreases with increasing depths and, as a result, the other terms ($m = 1, 2$) that are relatively constant with depth become more prominent in the total coseismic gravity change.

3.1. Moment Dip Trade-off

[29] It has been long known in the seismological community that the inversion of seismic moment tensors suffers a singularity for shallow sources [e.g., *Kanamori and Given*, 1981]. This is due to the fact that the dipolar coefficient K_1, proportional to the shear stress y_4, vanishes at the surface with the result that the two components $M_{r\varphi}$ and $M_{r\theta}$ do not excite seismic modes at or near the surface. Conversely, they cannot be resolved for a surficial source (or are poorly resolved for a shallow source) from seismograms. This classical singularity results in a trade-off between scalar moment M_0 and dip angle δ.

[30] For thrust earthquakes ($\lambda \approx 90°$), the observations of isotropic ($m = 0$) and quadrupolar ($m = 2$) gravity response (equations (6a) and (6d)) constrain only $M_0 \sin 2\delta$. The complementary information required to separate the scalar

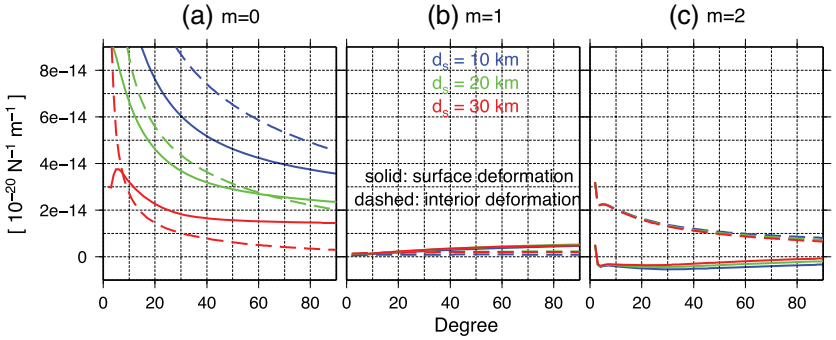

Figure 3. Same as Figure 1, with function $F_m(d_s)$ separated into their surface ($F_m^{(B)}$) and interior ($F_m^{(I)}$) contributions to the total gravitational potential. Note that the sign of $F_0^{(B)}$ (shown as solid line) has been reversed in Figure 3a for plotting clarity.

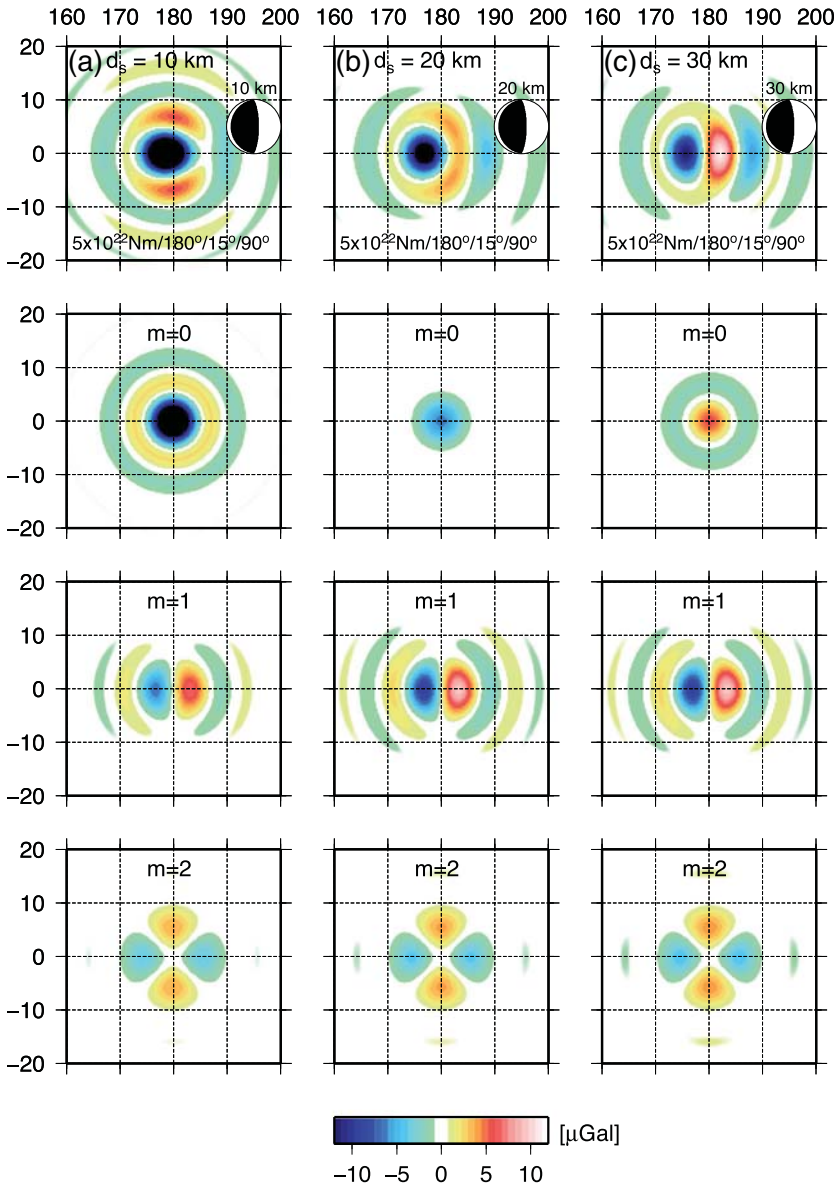

Figure 4. Examples of synthetic gravity changes from a double-couple seismic source at different depths with the layered Earth model are shown in the top panels. The focal mechanism parameters are given by $M_0 = 5.0 \times 10^{22}$ N m, $\phi_f = 180°$, $\delta = 15°$, and $\lambda = 90°$. The source is located at the center of each diagram within the upper crust (10 km), lower crust (20 km), and upper mantle (30 km). The lower panels show the contribution to the total gravity change Figures 4a–4c from each order ($m = 0$, 1, and 2, respectively).

moment M_0 and dip δ comes from the observations of the dipolar ($m = 1$) gravity response (equation (6c)) containing a factor of $M_0 \cos 2\delta$. The resolvability of M_0 and δ from (noisy) gravity measurements would, therefore, be dependent on the ratio of $S_{l,1}$ (and $C_{l,1}$ depending on strike) to $C_{l,0}$. Taking a reasonable range for shallow-dip events ($5° \le \delta \le 30°$), the ratio is approximately given by

$$O\left(\left|\frac{S_{l,1}}{C_{l,0}}\right|\right) \approx O\left(\left|\frac{\sum_n K_1(d_s) y_5(a)}{\sum_n \frac{1}{2} K_0(d_s) y_5(a)}\right|\right),$$

which is expected to go to zero with all K_1 coefficients at the surface. Assuming that the accuracy of satellite gravity measurements depends only on degree l, the signal-to-noise ratio (SNR) of $S_{l,1}$ and $C_{l,0}$ can be related through:

$$\frac{\mathrm{SNR}\{S_{l,1}\}}{\mathrm{SNR}\{C_{l,0}\}} \approx 2\left|\frac{F_1(d_s, l)}{F_0(d_s, l)}\right|. \tag{11}$$

[31] Figure 5 presents the ratios (11) for various source depths. As expected and by the analogy with seismological inversions [*Kanamori and Given*, 1981], for very shallow sources, this ratio remains small over the entire bandwidth ($l \le 50$) accessible by the GRACE satellites. At such shallow depths the dipolar term ($m = 1$) is simply too poorly excited to resolve both M_0 and δ from a noisy large-scale satellite gravity dataset. However, for other sources within the lower

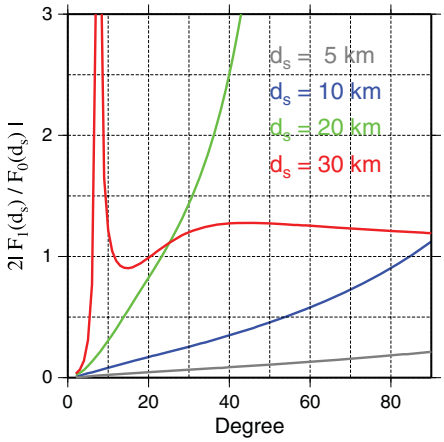

Figure 5. Ratio of the dipolar gravity response $F_1(d_s)$ to the isotropic response $F_0(d_s)$ as function of degree l. This ratio characterizes the resolvability of moment from dip angle when inverting gravity observations, as a function of degree l for various source depths.

crust and the upper mantle, SNR$\{S_{l,1}\}$ becomes comparable to SNR$\{C_{l,0}\}$, likely allowing the resolution of M_0 and δ from the GRACE gravity observations.

4. Observations of Global Gravity Field and Spatial Localization

[32] As part of the GRACE project, one month's worth of orbital tracking data of the GRACE satellites have been routinely analyzed to obtain an "average" snapshot of the global gravity field at each month since April 2002. Such a snapshot is represented by and provided as a set of spherical harmonic coefficients, known as L2 product. In this study, we will examine those L2 spherical harmonic coefficient data from April 2002 to September 2012. The L2 data have been continuously updated with the improved processing strategy and background models including atmosphere and ocean variability. We used the most recent Release-5 (RL5) L2 data product except for 2002, for which the Release-4 (RL4) product was used, since the RL5 product has, at present, not yet been processed for these years [*Bettadpur et al.*, 2012].

[33] The coseismic gravitational perturbation tends to be spatially localized around the epicenter, and thus, its energy is smeared out among all spherical harmonic coefficients. Due to other gravitational variations from continental-scale mass variations (mainly in association with seasonal climate changes), the earthquake signal may not be apparent directly from the L2 data. Such "local" signal can be better delineated from the "global" spherical harmonic coefficients by applying a spatial window around the region of interest. *Simons et al.* [1997] and *Wieczorek and Simons* [2005] developed an optimal windowing function to extract the spatially confined signal by minimizing the spatial truncation (leakage) effect. *Han and Simons* [2008] applied this technique successfully to identify the 2004 Sumatra-Andaman earthquake signal out of the spherical harmonic coefficients from GRACE. *Han and Ditmar* [2008] discussed how the SNR of non-stationary signals may be substantially underestimated, if not localized, and suggested a better way to quantify the SNR of the local signal from the spherical harmonic coefficient data under stationary noise.

[34] The optimal spatial windowing function $h(\theta)$, often isotropic and band-limited, is found by maximizing its energy within a confined region of interest [*Wieczorek and Simons*, 2005]. Once the windowing function is determined, one can obtain spherical harmonic coefficients of the spatially localized signals using a "convolution-like" formula provided in equation (10) of *Wieczorek and Simons* [2005] and given as:

$$C^h_{lm} = (-1)^m \sum_{j=0}^{L_h} \sum_{i=|l-j|}^{l+j} h_j \, C_{im} \sqrt{(2i+1)(2j+1)(2l+1)} \begin{pmatrix} i & j & l \\ 0 & 0 & 0 \end{pmatrix} \begin{pmatrix} i & j & l \\ m & 0 & -m \end{pmatrix}, \tag{12}$$

where L_h is the maximum expansion degree of the windowing function and h_j is the expansion coefficients of the zonal (isotropic) window $h(\theta)$. The last two parentheses are Wigner-3j functions. C_{im} is the (original) spherical harmonic coefficient and C^h_{lm} is the localized coefficient highlighting the signals over the region.

[35] As implied by equation (12), the coefficient of the localized (or windowed) signal is nothing but a linear combination of the original coefficients with the weights defined by the choice of the windowing function. The localized coefficient of degree l is computed with the original coefficients within the bandwidth $[\max(0, l - L_h), (l + L_h)]$. If the original signal is known only to a certain degree such as L_s, it can be readily seen from the upper bound of the summation in equation (12) that the permissible range of the localized coefficients is limited to $L_s - L_h$. Also the windowed spectra of the low degrees ($l < L_h$) can be biased as noted in Section 5.1 of *Wieczorek and Simons* [2005]. Therefore, we use the localized spherical harmonic coefficients within the bandwidth, $L_h + 1$ to $L_s - L_h$, from monthly GRACE L2 data.

[36] Figure 6 shows signals for recent great earthquakes (the 2004 Sumatra-Andaman, 2007 Bengkulu, 2010 Maule (Chile), 2011 Tohoku-Oki, and 2012 Indian Ocean events) that are in a detectable range with GRACE gravity data. The spatial maps of coseismic gravity change computed from Global Centroid Moment Tensor (GCMT) solutions of each respective event are shown in Figures 6a-6e, with the spherical circle that delineates the area of localization with the spherical cap of radius θ_h. The cross section of each spatial windowing function is shown in Figures 6f–6j, respectively. The relative amplitude is presented over the spherical angular distance θ from the center of the cap. The expansion degree L_h is fixed at 20 and the cap radius θ_h is chosen to capture most of the (expected) coseismic gravity signal, mainly depending on the size of the earthquake. This provides the only optimally localized windowing function for each earthquake (that is, the Shannon number is equal to 2 as in *Wieczorek and Simons* [2005]). The amplitude of each windowing function becomes approximately 1% of the maximum amplitude beyond the spherical cap of radius θ_h, indicating that $h(\theta)$ is nearly perfectly concentrated within the spherical cap. The concentration ratio γ, showing how much power of the window function is concentrated within the spherical cap, approaches 99% for all cases.

[37] The temporal variability (in terms of root-mean-square, RMS) of the monthly GRACE L2 data, after localization is applied in the respective areas, is shown in Figures 6k–6o,

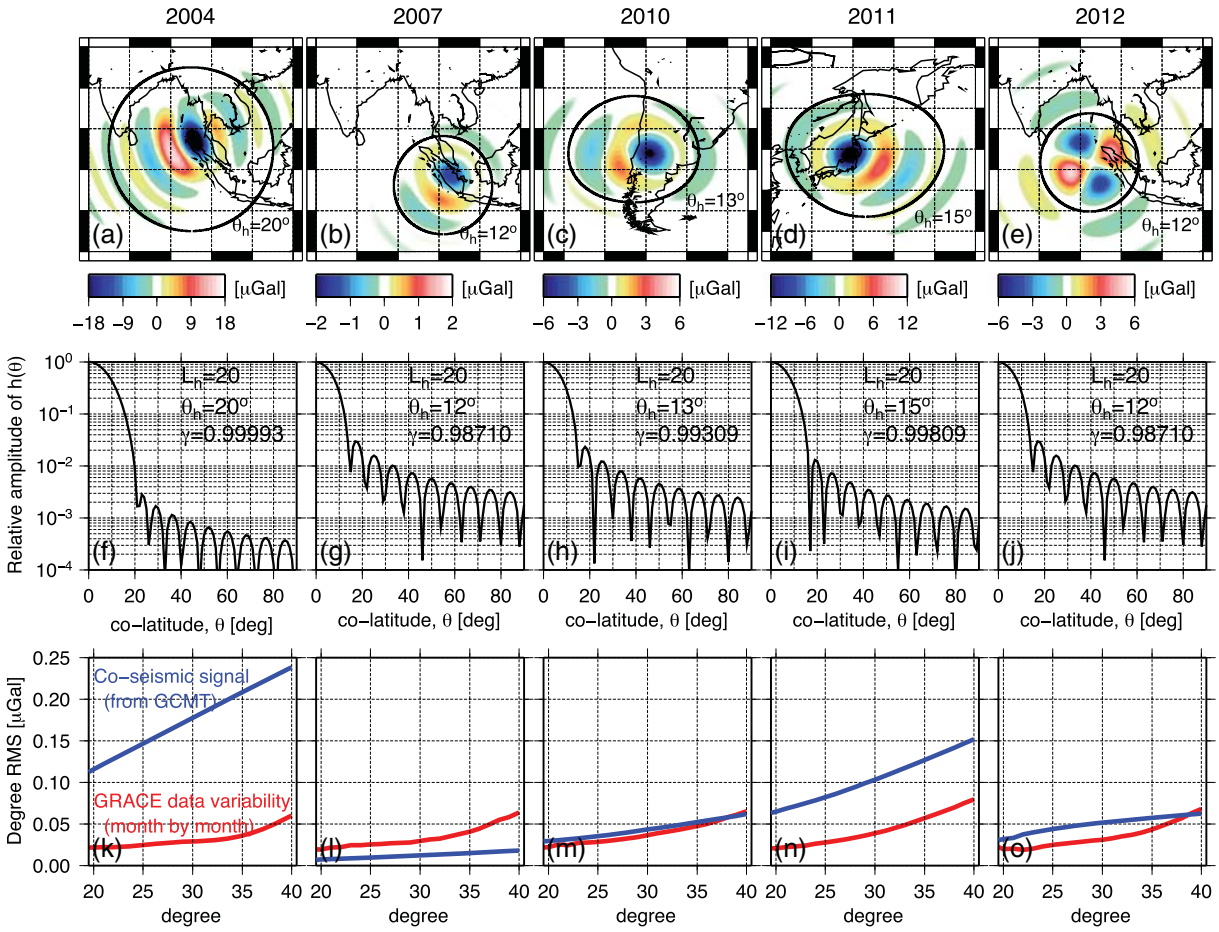

Figure 6. (a–e) Synthetic gravity changes computed from centroid moment tensor (CMT) solutions for the 2004 Sumatra-Andaman, 2007 Bengkulu, 2010 Maule, 2011 Tohoku-Oki, and 2012 Indian Ocean earthquakes, respectively. The black circle delineates the spherical cap of radius θ_h as the region of localization where the spatial windowing function $h(\theta)$ is concentrated; (f–j) cross sections showing the relative amplitude of $h(\theta)$, expanded to degree 20 ($L_h = 20$), but with a different cap radius (θ_h) for each event; (k–o) degree RMS spectrum (square root of power spectrum in μGal) of synthetic coseismic gravitational potential (blue line) and of average variability of monthly GRACE L2 data (red line) after applying an identical spatial windowing function in each region. The data variability (red line) includes the gravity signal variability (e.g., seasonal change) as well as the GRACE instrument noise. The ratio of the (predicted) coseismic gravitational perturbation to the GRACE data variability approaches 6, 0.5, 1, 3, and 1.5, respectively for each event.

for each earthquake, within the bandwidth, $L_h + 1$ to $L_s - L_h$ (i.e., from 21 to 40 in our case since $L_s = 60$ and $L_h = 20$). This is suggestive of inherent temporal variability of the gravity field (mass redistribution) in each region and of the observational noise. The gravity signal strength predicted from GCMT solution of each event is also depicted after the same localization is applied. The ratio of the (predicted) coseismic gravitational perturbation to the GRACE data variability approaches 6, 0.5, 1, 3, and 1.5, respectively for each event, within most of the bandwidth from degrees 21 to 40. In Section 6, we will examine the time series of these localized L2 coefficient observations and invert them to determine the fault parameters of each earthquake.

5. Linear and Nonlinear Inversion

[38] So far, we examined the forward model of the gravitational potential change in response to a point-source double-couple, expressed in terms of the moment tensor as in equation (6) and in particular, its dependence on depth. The spatial localization of global GRACE gravitational potential data was introduced for identifying and analyzing coseismic gravity changes around various earthquake regions. In this section, we discuss how we determine the moment tensor from the "localized" GRACE data and, subsequently, invert the double-couple source parameters from the moment tensor solutions.

5.1. Linear Estimation of Moment Tensor from Gravity Data

[39] The estimation of the moment tensor components from a series of geopotential observations is straightforward due to its linearity, when the data are expressed in terms of a series of spherical harmonic coefficients, as discussed in Section 2. In order to invert the dataset of localized GRACE gravitational potential coefficients into the moment tensor **m**,

we express the forward problem as a succession of three operations.

[40] First, as expressed in equation (6), we multiply the tensor of Green's functions evaluated at the seismic source depth d_s by the moment tensor:

$$\mathbf{X}^s = \mathbf{F}(d_s)\mathbf{m}, \tag{13}$$

where $\mathbf{F}(d_s)$ regroups, for all used values of l, the five functions F_m discussed in Section 3; $\mathbf{m} = (M_{rr}, M_{r\theta}, M_{r\phi}, M_{\theta\theta} M_{\phi\phi} - M_{\theta\phi})$ represents the five independent unknown moment tensor components; the resulting vector $\mathbf{X}^s$ regroups, for all values of l, the spherical harmonic coefficients in equation (6). Second, we apply the rotations expressing the change of frames, and obtain

$$\mathbf{X}^g = \mathbf{R}(\theta_s, \phi_s)\mathbf{X}^s, \tag{14}$$

where the dimension of the vector $\mathbf{X}^g$ is the sum of $(2l+1)$ over the range [*lmin*, *lmax*] used in the inversion, and $\mathbf{R}$ (θ_s,ϕ_s) is a rotation matrix consisting of all the elements $E^l_{m,i}$ of equation (7). Third, the spatial localization discussed in Section 4 is applied, leading to

$$\mathbf{X}^L = \mathbf{L}(\theta_s, \phi_s)\mathbf{X}^g, \tag{15}$$

where $\mathbf{L}(\theta_s,\phi_s)$ is a matrix expressing the operation in equation (12).

[41] At this point, $\mathbf{X}^L$ regroups the gravitational potential coefficients expressed in the geographic frame, and localized around the epicenter (θ_s,ϕ_s), as excited by the double-couple source described by $\mathbf{m}$. The inversion then consists of using the GRACE dataset of observed coseismic change in gravitational potential $\mathbf{x}$ (itself expended onto spherical harmonics) to solve for $\mathbf{m}$ through

$$\mathbf{L}(\theta_s, \phi_s)\mathbf{x} = \mathbf{L}(\theta_s, \phi_s)\mathbf{R}(\theta_s, , \phi_s)\mathbf{F}(d_s)\mathbf{m} + \mathbf{e}, \tag{16}$$

where $\mathbf{e}$ is the noise in the GRACE dataset. Note that $\mathbf{L}$ appears on both sides of (16) because $\mathbf{e}$ is determined only when the localized data $\mathbf{Lx}$ is sought from noisy time series of GRACE data. Finally, simple least squares is used to determine the estimate of the moment tensor components, $\hat{\mathbf{m}}$, and its covariance matrix, $\mathbf{C}\{\hat{\mathbf{m}}\}$.

5.2. Nonlinear Estimation of Double-Couple From Moment Tensor

[42] The determination of double-couple source parameters (i.e., M_0, ϕ_f, δ, and λ) from moment tensor components consists of solving backwards the equations in (6). While point-source double-couples are characterized by four parameters, they do not constitute a four-dimensional vector space, and moment tensor inversions have to be carried out in a five-dimensional vector space, fostering both nonlinearity and non-uniqueness. We use a standard approach in seismology to derive two nodal plane solutions of strike, dip, and rake by using a computer code (bb.m, a Matlab code written by Oliver Boyd, based on mij2d.f, a FORTRAN code by Chen Ji) available from the website [www.ceri.memphis.edu/people/oldboyd/Software/Software.html]. They are used as initial solutions for our refined inversion considering variable uncertainties in moment tensor components as described below.

[43] First of all, we examine correlation among the fault parameters. For low-dip ($\delta \approx 0$) earthquakes as in most of cases in this study, the moment tensor components are approximated (to the first order) to $M_{rr} \approx M_0 2\delta \sin\lambda$, $M_{r\theta} \approx -M_0 \cos(\phi_f - \lambda)$, $M_{r\phi} \approx M_0 \sin(\phi_f - \lambda)$, $M_{\theta\theta} - M_{\phi\phi} \approx -M_0 2\delta \sin(2\phi_f - \lambda)$, and $M_{\theta\phi} \approx -M_0\delta \cos(2\phi_f - \lambda)$. It indicates $M_{r\theta}$ and $M_{r\phi}$ would be dominant and $\phi_f - \lambda$ (not individually) would be better-constrained from the moment tensor. The parameters such as ϕ_f and λ would be tightly coupled in a manner that $\phi_f - \lambda$ is constant. *Han et al*. [2011] discussed this trade-off between strike and rake found from various seismic solutions and GRACE data inversion for the 2011 Tohoku-Oki earthquake.

[44] The correlation among double-couple parameters can be quantified by examining a covariance matrix of the double-couple solution. We derive it by introducing a small perturbation in the double-couple parameters as follows:

$$M_0 = \widetilde{M}_0(1 + d\eta), \tag{17a}$$

$$\phi_f = \widetilde{\phi}_f + d\phi_f, \tag{17b}$$

$$\delta = \widetilde{\delta} + d\delta, \tag{17c}$$

$$\lambda = \widetilde{\lambda} + d\lambda. \tag{17d}$$

[45] The perturbation in the vector of moment tensor components $\Delta\mathbf{m}$ due to perturbation in double-couple parameters $\mathbf{d}$ is simply written as $\Delta\mathbf{m} \approx \mathbf{Bd}$, where $\mathbf{B}$ is a matrix consisting of partial derivatives, e.g., $\frac{dM_{rr}}{d\eta}$, $\frac{d(M_{\theta\theta} - M_{\phi\phi})}{d\delta}$, evaluated for nominal values of $\widetilde{M}_0$, $\widetilde{\delta}$, $\widetilde{\lambda}$, and $\widetilde{\phi}_f$. The $\Delta\mathbf{m}$ includes, e.g., ΔM_{rr}, and$\Delta(M_{\theta\theta} - M_{\phi\phi})$, and finally $\mathbf{d}$ consists of $d\eta$, $d\delta$, $d\lambda$, and $d\phi_f$. Therefore, the covariance matrix of the double-couple parameters, $\mathbf{C}\{\hat{\mathbf{d}}\}$, is computed from the covariance matrix of the moment tensor solution, $\mathbf{C}\{\hat{\mathbf{m}}\}$, by error propagation:

$$\mathbf{C}\{\hat{\mathbf{d}}\} = \left[\mathbf{B}^T\left[\mathbf{C}\{\hat{\mathbf{m}}\}\right]^{-1}\mathbf{B}\right]^{-1}. \tag{18}$$

[46] The correlation matrix is simply computed by rescaling all elements of $\mathbf{C}\{\hat{\mathbf{d}}\}$ by $\rho_{i,j} = c_{i,j}/\sqrt{c_{i,i}c_{j,j}}$, where $c_{i,j}$ is a component of the i-th row and j-th column of the matrix. This is a metric we examine using the initial fault plane solutions from moment tensor estimates for all earthquakes in this study.

[47] The (iterative) least square refinement to the initial solution of $\widetilde{M}_0$, $\widetilde{\delta}$, $\widetilde{\lambda}$, and $\widetilde{\phi}_f$, (available from the eigenvalue and eigenvector decomposition of the moment tensor matrix, i.e., from the code bb.m), is found by $\hat{\mathbf{d}} = \mathbf{C}\{\hat{\mathbf{d}}\}\mathbf{B}^T \left[\mathbf{C}\{\hat{\mathbf{m}}\}\right]^{-1}(\hat{\mathbf{m}} - \widetilde{\mathbf{m}})$ where $\widetilde{\mathbf{m}}$ is a moment tensor component vector computed with the initial double-couple parameters. This solution takes care of the variable uncertainties and correlation in the moment tensor estimates from GRACE. Depending on the correlation structure among four parameters computed with equation (18), this solution may need to be constrained. We will elaborate on this procedure for each of the earthquakes in Section 6.

[48] We do not attempt to solve for the centroid location (θ_s,ϕ_s) and depth d_s because their dependence on gravity

data, as expressed in equation (16), is algebraically complex. However, we test various depths d_s, and at each depth, we solve for the corresponding moment tensor and the best double couple. We adopt the centroid location (θ_s,ϕ_s) determined from other seismic CMT or finite fault solutions.

6. Inversion for Moment Tensor and Fault Parameters

6.1. 2004 Sumatra-Andaman Earthquake

[49] We analyzed the entire time series of monthly global gravity fields from April 2002 to September 2012 (in terms of spherical harmonic coefficients) in order to separate, in the data obtained after the rupture, the gravity signal due to the earthquake from the background temporal variation in the gravity potential. We fit the time series using the mean, annual and semiannual sinusoids, and a Heaviside step (for coseismic) and a logarithmic function (for postseismic) simultaneously. The logarithmic term, $\log\left(1+\frac{t}{150\ \text{days}}\right)$ where t is the time elapsed since the rupture, is used to eliminate the effect of viscous mantle relaxation on a time scale significantly longer than that expected from a seismic source, even allowing for slow coseismic components. The linear and quadratic components were not included in the regression because they are correlated with the postseismic trends; however, the coseismic step estimates are not affected, regardless of whether the linear and quadratic components are included or not (by virtue of sufficiently long time series). In the time series regression, we did not use the data in 2012 to avoid any potential influence by the nearby 2012 strike-slip earthquakes.

[50] Figure 7 shows the time series of the GRACE L2 coefficients, localized within the domain shown in Figure 6a. The localized coefficient at degree l is computed with the neighboring coefficients, and thus creates correlation among the localized coefficients over degree (but independent over order), effectively reducing random noise in the original L2 data. For example, the localized coefficient at degree 30 was influenced by the original GRACE coefficients at degrees 10 to 50, because we used the windowing function expanded with the maximum degree 20 ($L_h = 20$). The (localized) coefficients were plotted in the (epicentral) coordinate system where the z axis locates at the center of the spatial window function (5.4°N, 93.8°E). It is the location where the largest moment was released according to the finite fault model used in *Han et al*. [2006]. In this rotated coordinate system, the gravity coefficients at orders 0, 1, and 2 are directly related to the moment tensor components of the centroid at the pole (i.e., 5.4°N, 93.8°E in a geographic coordinate system), as described in equation (6). Almost all coefficients between degrees 21 and 40 present large perturbations due to the earthquake in episodic change as well as gradual change afterwards. Although postseismic observations last long (>7 years), they need to be carefully examined since they might be affected by background gravity changes due to inter-annual climate variability. The longer postseismic time series reveal that they may be better modeled with a logarithmic function than the exponential function used in *Han et al*. [2008] for the analysis of only 2.5 years of postseismic data. The coseismic SNR is found highest from the coefficients of $C_{l,1}$, $S_{l,1}$, and $S_{l,2}$, for $M_{r\theta}$, $M_{r\phi}$, and $M_{\theta\phi}$, respectively, and degrades for $C_{l,2}$ and $C_{l,0}$, related to the diagonal components of the moment tensor, M_{rr} and $M_{\theta\theta}-M_{\phi\phi}$, respectively.

[51] The coseismic step and its error estimates for each of the localized coefficients were used for (linear) inversion of the moment tensor components $\hat{\mathbf{m}}$ and its covariance matrix, $\mathbf{C}\left\{\hat{\mathbf{m}}\right\}$. From the condition $M_{rr}+M_{\theta\theta}+M_{\phi\phi}=0$, we found three diagonal components. The GRACE estimates at depth of 20 km and GCMT are compared in Figure 8, indicating that GCMT provides smaller estimates of the components, particularly $M_{r\phi}$. The corresponding focal mechanism diagram (i.e., "beachball") was drawn by finding two fault planes using the program mentioned in Section 5.1. We use them only as initial solutions for our inversion of the double-couple parameters reflecting the error characteristics of the moment tensor estimates from GRACE.

[52] First of all, the correlation matrix as discussed in Section 5.2 was computed for both fault-plane solutions and shown in Figure 9. As suspected from the low dip fault plane, rake and strike are tightly coupled with nearly unity correlation, while the other fault plane solution does not yield such strong coupling between them. This pair of correlation characteristics is typical for other thrust events considered in this study (note, however, that the correlation matrix looks different for the strike-slip event that will be discussed later).

[53] Due to strong correlation between strike and rake, we fixed strike ϕ_f a priori and solved for M_0, δ, and λ simultaneously from the moment tensor and its covariance estimates following the procedure in Section 5.2. The convergence was always obtained within not more than three iterations. The solutions at various strikes for both fault planes are shown in Figure 10. By changing ϕ_f in 1° steps around the initial strike, we found that double-couple solutions for the primary fault plane with $320° \le \phi_f \le 360°$ fit equally well the GRACE observations. The rake parameter changes linearly with strike, while the other parameters of M_0 and δ are relatively constant. The trade-off between strike and rake is only found for the plane with low dip angle. For the conjugate fault plane, the secondary double-couple solution can be delineated with $\phi_f = 150° \pm 5°$, $M_0 \sim 750 \times 10^{20}$ N m, $\delta \sim 82°$, and $\lambda \sim 88°$.

[54] We tested sensitivity of the fault solutions to depth. In this case, we fixed the strike at 340° and changed depths within the lower and upper crust and upper mantle (i.e., from 10 to 30 km). The solutions in the crustal layers yielded variance reduction (VR) = 0.91–0.95, while for solutions in the upper mantle (not shown), VR = 0.70–0.75 was substantially lower (Figure 11). Any solution within the crustal layer fit GRACE observations equally well with the ones in the lower crustal layer being even better. With increasing depths, δ gradually increases, while M_0 decreases and λ is practically unchanged. The solutions at shallower depths, particularly within the upper crust, show larger changes in M_0 with the variation in δ or depth than do the deeper sources, as expressed by a steeper slope in the $d_s - M_0$ or $\delta - M_0$ plot in Figure 11. This indicates that M_0 is not robustly resolved for the upper crustal solutions. As expected, for shallow thrust earthquakes, $M_0 \sin 2\delta$ is better-constrained [*Kanamori and Given*, 1981; *Tsai et al*., 2011]. As depth increases (i.e., lower crust), however, the effect becomes less acute, and the resolution of M_0 and δ improves.

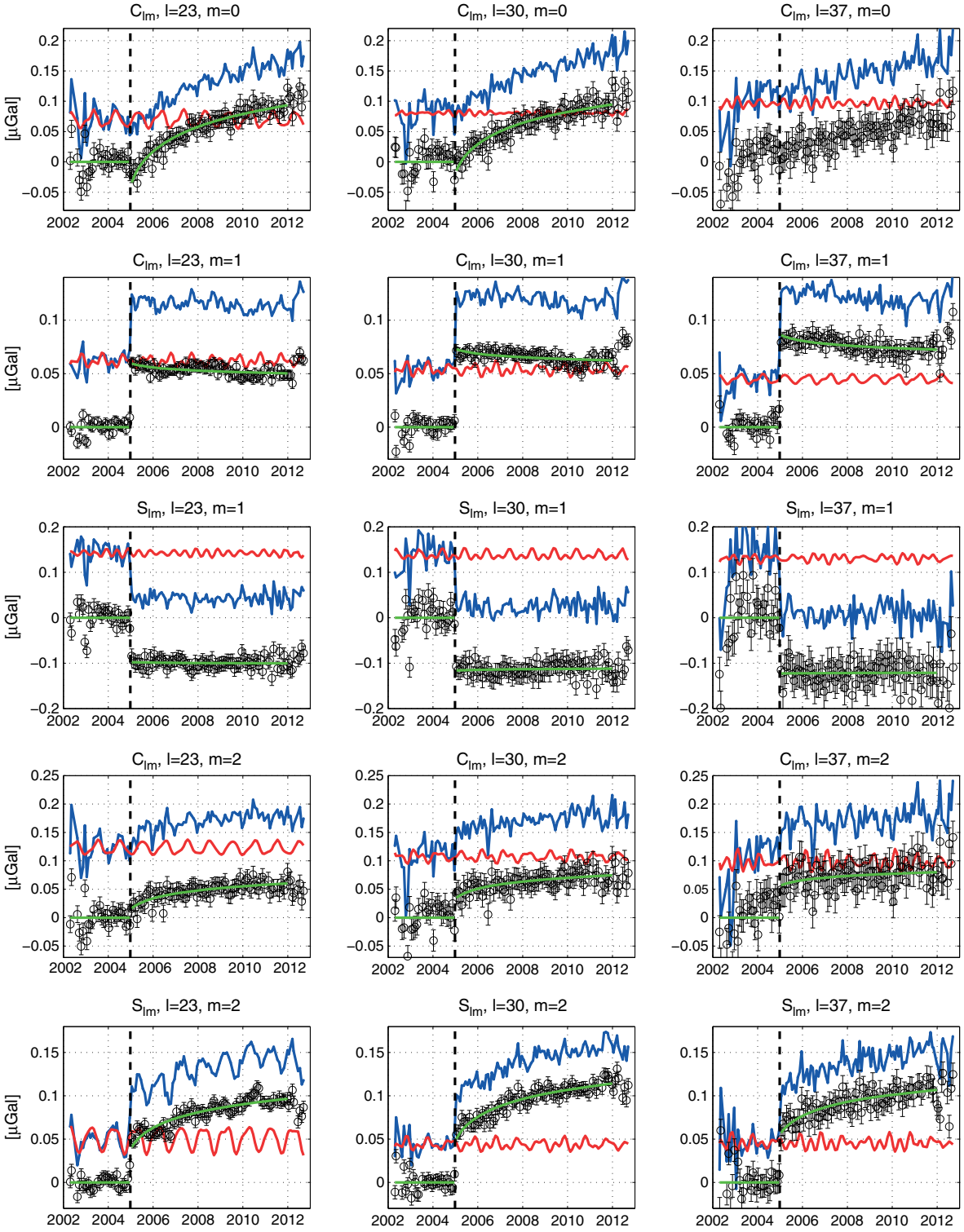

Figure 7. Monthly time series of the GRACE L2 data after applying the spatial localization over the Sumatra-Andaman earthquake region (solid blue line) and the seasonal and inter-seasonal fit (solid red line). Arbitrary offsets were added for clarity. The data residual (black line with error bars) was computed by subtracting the fit (red line) from the data (blue line). The associated error bar was estimated from the fit obtained between 2002 and 2011. The data residuals were subsequently analyzed using the Heaviside step and logarithmic functions for delineation of coseismic and postseismic changes, respectively (solid green line). The GRACE coefficients were rotated to the epicentral coordinate system where the z axis locates at 5.4°N and 93.8°E and the five lowest order ($m = 0$, 1, and 2; for both C_{lm} and S_{lm}) coefficients are shown at different degrees between 21 and 40. From the top to bottom, these coefficients related to the moment tensor components, M_{rr}, $M_{r\theta}$, $M_{r\phi}$, $M_{\theta\theta} - M_{\phi\phi}$, and $M_{\theta\phi}$, respectively.

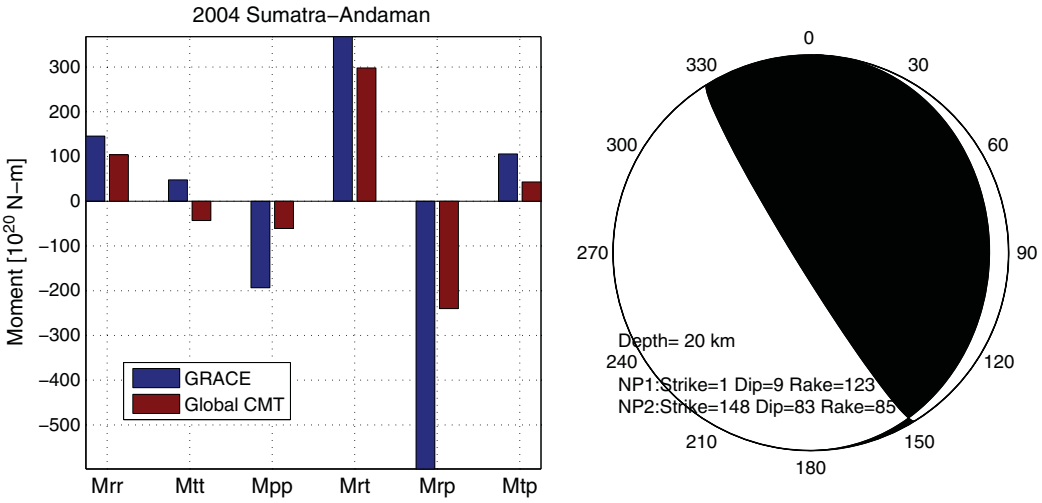

Figure 8. (left) The estimates of the moment tensor components of Mrr (M_{rr}), Mtt ($M_{\theta\theta}$), Mpp ($M_{\phi\phi}$), Mrt ($M_{r\theta}$), Mrp ($M_{r\phi}$), and Mtp ($M_{\theta\phi}$) from GRACE and GCMT. (right) For GRACE, the centroid depth was 20 km which is the focal mechanism corresponding to two possible fault planes (NP1 and NP2). This initial fault solution was computed from GRACE estimates of moment tensor without consideration of variable uncertainties in different tensor components.

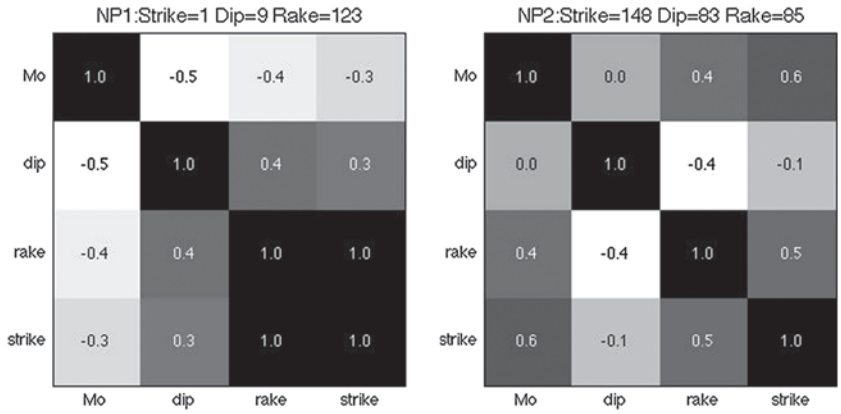

Figure 9. The correlation matrices of the fault (double-couple) parameter estimates for the two fault planes. Note nearly unity correlation between strike and rake for the fault plane (NP1) with a low dip angle.

[55] The single CMT solutions from GRACE at various depths within the crustal layers show scalar moments varying from 6.4 to 10×10^{22} N m and dip angles varying from 3° to 13°. This is a considerably higher estimate than the GCMT (4×10^{22} N m and a dip of 8°). In terms of amplitude and spatial pattern of gravity change (Figure 12), the GRACE solutions at various depths are all consistent, with differences smaller than 2 μGal at the spatial resolution of 500 km. The primary negative anomaly appears at the back-arc region and the secondary positive anomaly appears offshore.

[56] As a trial of multiple-source solutions, we introduced four centroids for the GRACE data analysis. We first determined the centroid locations corresponding to the major asperities based on a finite fault model [*Han et al*., 2006]. The fault parameters (M_0, δ, and λ) of each of the four centroids at a depth of 20 km were simultaneously estimated with strike fixed as 340° for all centroids and the dip angle was assumed to be uniform for the all centroids (that is, total nine independent parameters were estimated: four scalar moments, four rakes, and one dip for four centroids). Expectedly, the new solution with four sources shows improvement, yielding VR = 0.99. For the case of the multiple CMT solutions from GRACE, the total moment is 1160×10^{20} N m and the dip is 10°, producing a gravity change of similar (or slightly larger) amplitude as the single centroid solution, but elongated along strike with the rakes decreasing northward (Figure 13). The overall distribution of the moments with changing geometry (combination of strike and rake) in N-S direction is consistent with the five moment tensor solutions found from long-period seismic data [*Tsai et al*., 2005].

6.2. 2007 Bengkulu Earthquake

[57] This earthquake of moment 5×10^{21} N m ($M_w = 8.4$) [*Borrero et al*., 2009] is the smallest one that was detected by GRACE gravity data during the period from 2002 to 2012. The GCMT reports this event as a shallow-dip thrust rupture, striking $\phi_f = 327°$ at depth of 23.3 km. It released the largest moment (~40×10^{20} N m) in the component of

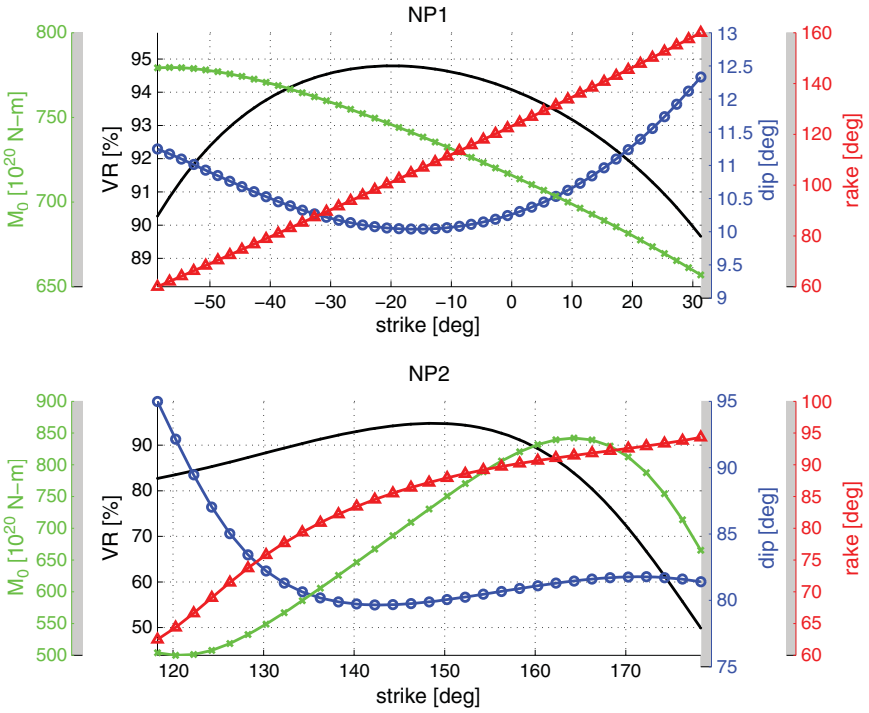

Figure 10. The fault plane solutions determined from the moment tensor and its error covariance estimates for both planes with various strikes. The depth was fixed as 20 km for all cases. In each case, the strike was fixed a priori and M_0, δ, and λ were estimated simultaneously. The solutions with strike ranging between 320° and 360° are acceptable with VR $\geq$ 0.94 for the primary fault plane and the ones with strike from 145° to 155° are acceptable for the secondary fault plane. Note that λ is linearly dependent of the strike while M_0 and δ are relatively consistent for the primary fault plane, as also predicted from the correlation matrix (Figure 9).

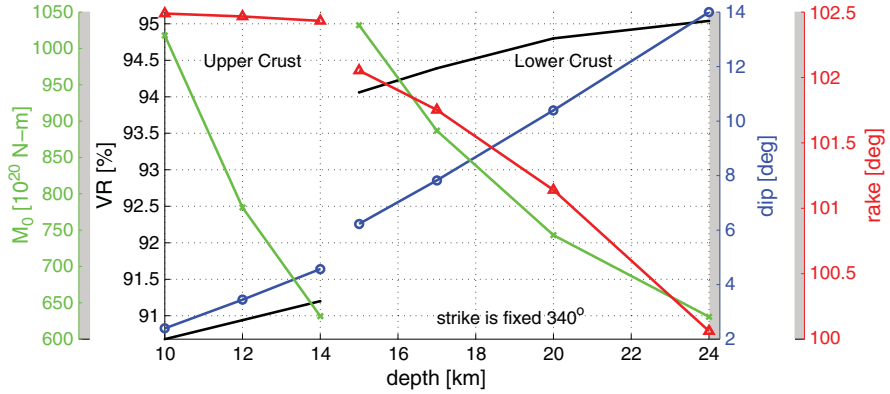

Figure 11. The fault plane solution at various depths within the crustal layers. The strike was fixed at 340° for all cases. In each case, depth was fixed a priori and the moment tensor was determined at the corresponding depth and then the double-couple parameters were estimated from it under the constraint $\phi_f = 340°$. The solutions with the centroid below the crustal layer do not fit the GRACE data. M_0 and δ are highly dependent on depth while λ is not.

$M_{r\theta}$. The 10 years of GRACE gravity time series localized over the region (Figure 6b) identified a statistically significant change in $C_{l,1}$ coefficients, before and after the earthquake epoch as shown in Figure 14. Such coseismic jump in the coefficients estimates the $M_{r\theta}$ moment release of $4.8 \pm 0.3 \times 10^{21}$ N m at a depth of 24 km, favorably comparing with the GCMT moment estimate. The second largest moment release ($\sim 2.5 \times 10^{21}$ N m) is expected from the $M_{r\phi}$ component; however, noisier $S_{l,1}$ coefficients of the GRACE gravity data make it difficult to identify this subtle change. GRACE satellites measure the gravity change in the N-S direction (controlled by $M_{r\theta}$) much better than in the E-W direction (controlled by $M_{r\phi}$) due to their better sampling of along track orbit perturbation [*Han et al.*, 2005].

[58] The 2005 Nias earthquake ruptured 3 months after the 2004 Sumatra-Andaman earthquake and had a moment

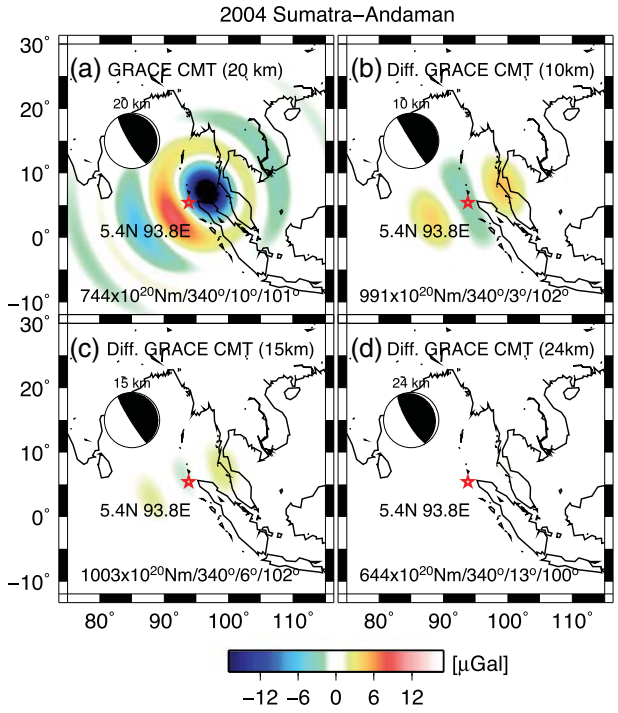

Figure 12. (a) Surface gravity changes computed from the GRACE solution for the 2004 Sumatra-Andaman earthquake, at a spatial resolution of 500 km (or spherical harmonic degree up to 40). The particular solution with the centroid depth of 20 km was used. (b–d) Difference in surface gravity between the solution at 20 km depth and the ones at 10, 15, and 24 km, respectively. The estimates of scalar moment, strike, dip, and rake for each solution are presented at the bottom of each panel. The location of the centroid is 5.4°N and 93.8°E.

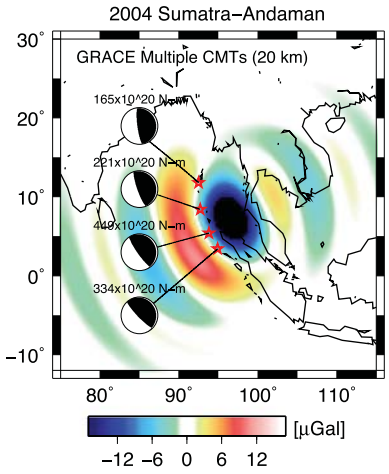

Figure 13. Same as Figure 12a for the 2004 Sumatra-Andaman earthquake multiple centroid solutions at a depth of 20 km. Total gravity change from four centroid moment tensors estimated from GRACE. The strike was fixed at 340° for all centroids and the dip is assumed to be the same for all centroids. The individual location of the centroids (shown as red star) were determined by approximating the finite fault model used in *Han et al.* [2006]. They are (3.4°N, 94.9°E), (5.4°N, 93.8°E), (8.4°N, 92.7°E), and (11.8°N, 92.5°E). Note that the overall distribution of the scalar moment and rake (or strike) northward is consistent with the long-period seismic solutions found in *Tsai et al.* [2005].

magnitude twice as large as the 2007 event (110×10^{20} N m). However, this event was difficult to separate in the monthly GRACE data after the large coseismic and postseismic gravity change of the 2004 Sumatra-Andaman earthquake.

6.3. 2010 Maule (Chile) Earthquake

[59] A localization of the GRACE L2 time series in the Chilean region (Figure 6c) reveals coseismic and (possibly) postseismic gravity changes in association with the 2010 Maule earthquake (Figure 15). It effectively diminishes other signals and highlights the gravity variations confined to the specific region, including seasonal and inter-annual trends. This seasonal and inter-annual gravity change was removed as in the previous case. The residuals were then analyzed with the coseismic step and postseismic logarithmic functions. Likewise, the estimates of the coseismic step and its error from the localized coefficients within the degree band ($l = 21 - 40$) were used for the moment tensor and fault parameter inversion.

[60] The estimated moment tensor components from GRACE are compared with other seismic solutions in Figure 16. For this earthquake, the moment release in $M_{r\phi}$ (or $S_{l,1}$ coefficients) is much larger than $M_{r\theta}$ (or $C_{l,1}$ coefficients), indicating an overall strike along N-S. Compared to seismic solutions, GRACE overestimates M_{rr} and $M_{\theta\theta}$. The fault plane solutions and focal mechanisms are depicted on Figure 16, using the moment tensor estimates at a depth of 20 km. As in the previous case, these initial double-couple (fault) solutions were derived without considering variable uncertainties in the moment estimates. We also found that the correlation matrix for the low-dip fault plane (primary one) shows a tight coupling between strike and rake while the conjugate plane with larger dip does not, just like for the 2004 Sumatra-Andaman earthquake.

[61] Our final double-couple solutions considering the error covariance of the moment tensor estimates were determined by nonlinear inversion starting with the initial solutions. Figure 17 shows various solutions for two fault planes at depth of 20 km with variable strikes that are fixed a priori prior to each inversion. If we delineate the solutions yielding VR ≥ 0.88, M_0 varies between 215 and 222×10^{20} N m (deceasing with strike), δ varies between 17° and 20° (increasing with strike), and rake changes linearly between 80° and 115° (increasing with strike), when ϕ_f changes from 5° to 35°. The conjugate fault solution can be described with $M_0 = 220 \pm 7 \times 10^{20}$ N m, $\delta = 72° \pm 2°$, $\lambda = 85° \pm 3°$, when $\phi_f = 185° \pm 7°$.

[62] The GRACE solutions at depths in the upper mantle (25–30 km) indicate poor agreement with the GRACE observations, yielding only VR $< 40\%$; on the other hand, the inversions in the upper and lower crust (10–24 km) yield VR $\sim 90\%$. The GRACE solutions obtained within the crustal layers are presented in Figure 18. As in the previous case, M_0 and δ change significantly with depth while λ is more or less constant. The depths of the Maule earthquake seismic solutions range from 24 to 35 km. The crustal thickness from CRUST 2.0 [*Bassin et al.*, 2000] over the Maule area is 32 km, thicker than the PREM model we

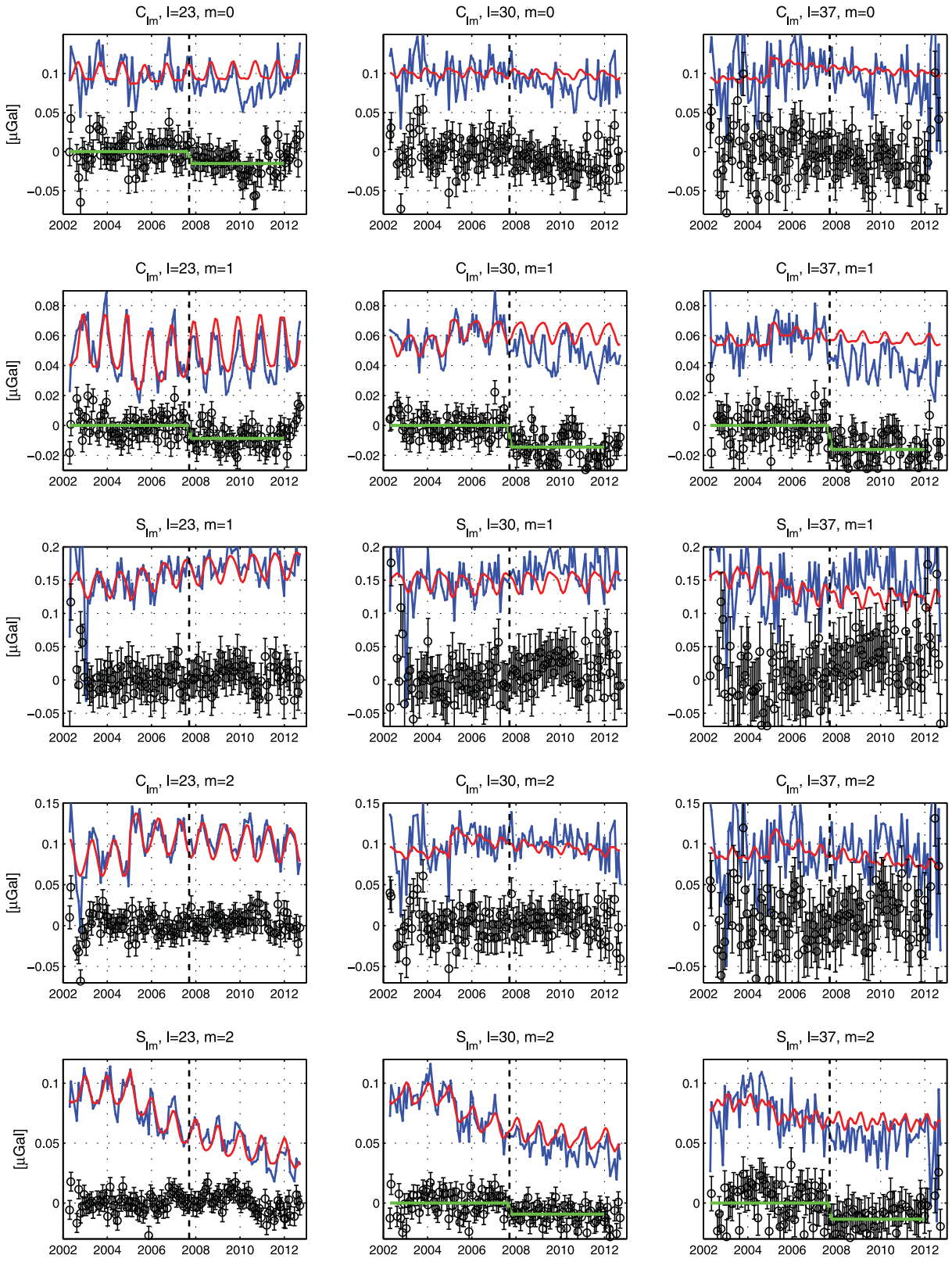

Figure 14. Same as Figure 7 for the 2007 Bengkulu earthquake. Note that the $C_{l,1}$ coefficients present a significant step before and after the epoch of the event in 2007. This particular earthquake was strongest in the component of $M_{r\theta}$.

used. Therefore, the GRACE solutions at the lower bound of the lower crust would be preferable. This particular solution is also consistent with most of other solutions in terms of the dip angle and moment [*Lay et al.*, 2010;

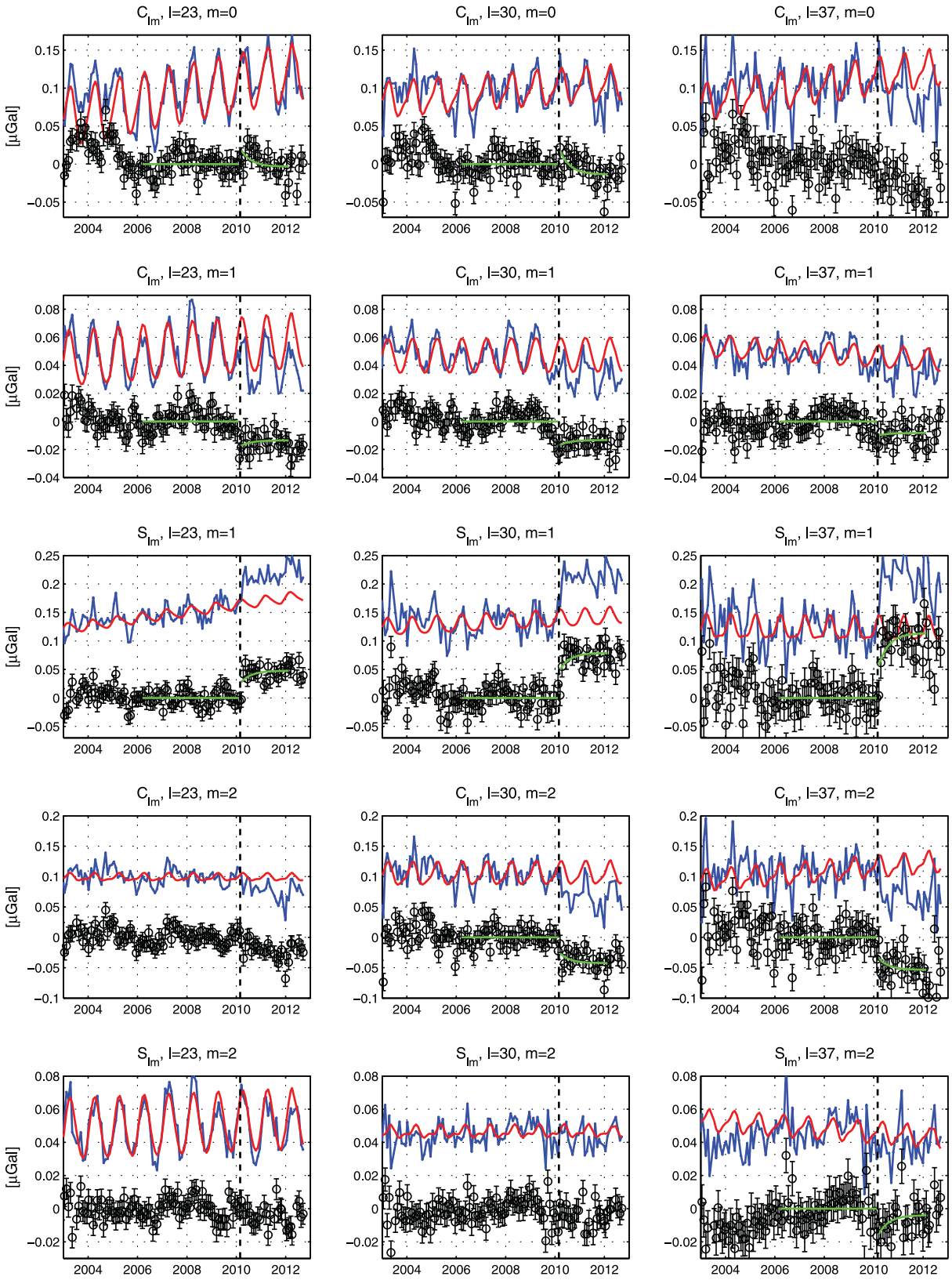

Figure 15. Same as Figure 7 for the 2010 Maule (Chile) earthquake. The GRACE coefficients were rotated in the coordinate system where the *z* axis locates at 35.6°S and 286.9°E.

G Shao et al., Preliminary Slip Model of the Feb 27, 2010 Mw 8.9 Maule, Chile Earthquake, 2010, http://www.geol.ucsb.edu/faculty/ji/big_earthquakes/2010/02/27/chile_2_27.html;

G. P. Hayes 2010, Finite Fault Model, Updated Result of the Feb 27, 2010 Mw 8.8 Maule, Chile Earthquake, http://earthquake.usgs.gov/earthquakes/eqinthenews/2010/

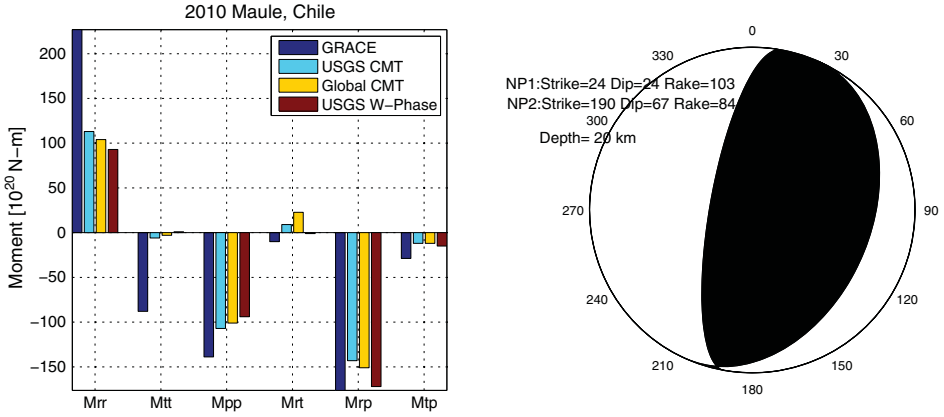

Figure 16. Same as Figure 8 for the 2010 Maule (Chile) earthquake.

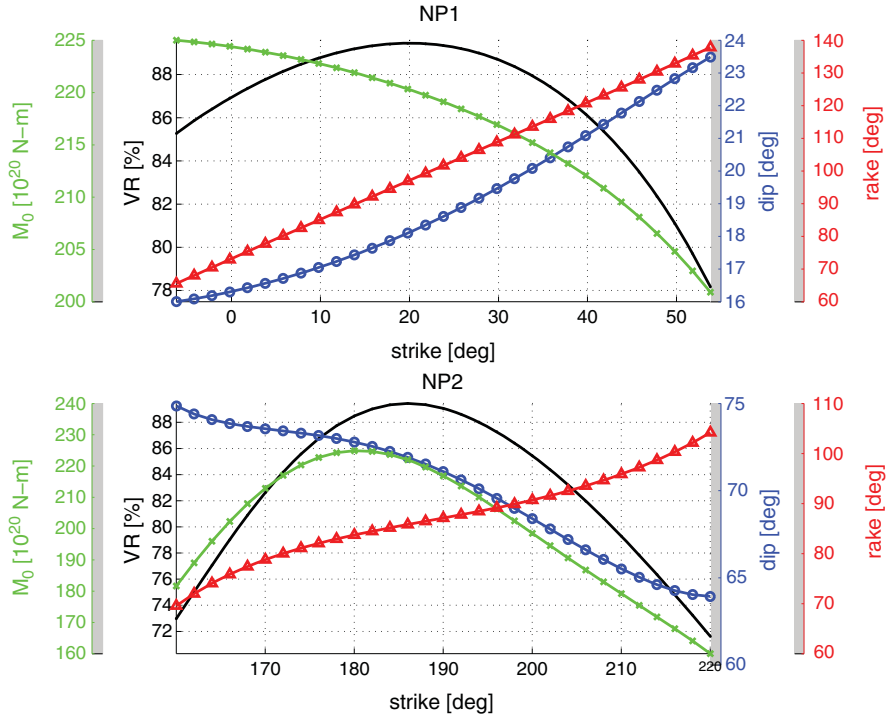

Figure 17. Same as Figure 10 for the 2010 Maule (Chile) earthquake. The depth was fixed as 20 km for all cases. The solutions with strike ranging from 5 to 35° are acceptable, with VR ≥ 0.88 for the primary fault plane and the ones with strike from 182° to 192° are acceptable for the secondary fault plane.

us2010tfan/finite_fault.php]. Also, the GRACE solutions show M_0 consistently larger than for other long-period point-source CMT solutions, agreeing better with the finite fault models. The GRACE solutions within the upper crust fit the observations equally well; however, the estimate of M_0 $\sin 2\delta$ is smaller than that of the solutions within the lower crust presumably due to the influence of a lower rigidity. The GRACE solutions within the upper crust layer, although presented with large variations in M_0, are more robust in terms of $M_0 \sin 2\delta$.

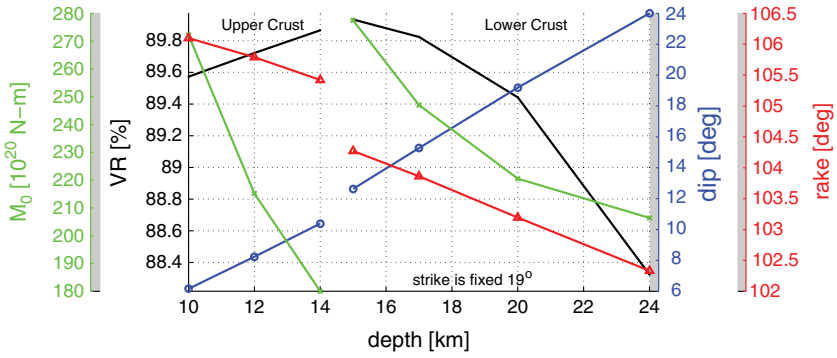

Figure 18. Same as Figure 11 for the 2010 Maule (Chile) earthquake. The strike was fixed at 19° for all cases.

[63] The gravity change was computed using the GRACE CMT solution at a depth of 24 km (Figure 19). It shows, likewise, the primary, negative, anomaly on land (back-arc region) and secondary, positive, anomaly offshore. The differences in terms of gravity (at 500 km resolution) among the solutions at depths of 10, 15, and 20 km are less than 1 μGal, while the dip angle estimates vary from 6 to 24° and the moment estimates from 207 to 276×10^{20} N m, depending on depth.

[64] For this event, we note that the lateral surface density heterogeneity due to the South American continent (being different from the uniform ocean layer used in our calculation) might be important. We made some *ad hoc* computations to roughly quantify the effect of land by combining the ocean anomaly computed with the uniform ocean layer and the land anomaly computed without the ocean layer. The eigenfunctions were computed using two different 1D Earth models with and without the ocean layer. We found the lateral heterogeneity may cause a difference in the negative gravity on land by 2 μGal at maximum. We defer more reasonable assessment of the surface heterogeneity in gravity to the computation of eigenfunctions with a 3D Earth model and sea level equation such as in *Broerse et al*. [2011].

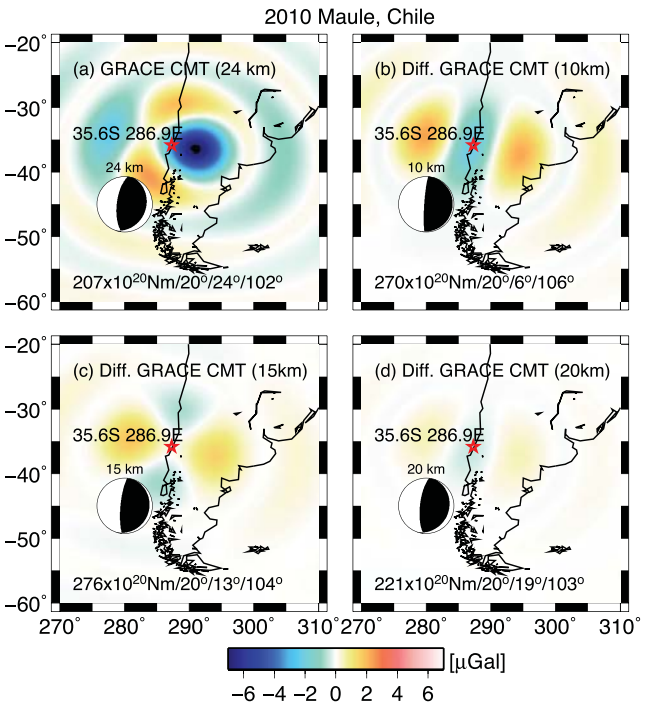

Figure 19. Same as Figure 12 for the 2010 Maule (Chile) earthquake. The location of the centroid is 35.6°S and 286.9°E.

6.4. 2011 Tohoku-Oki (Japan) Earthquake

[65] Figure 20 presents the time series of the same GRACE L2 coefficients, but localized around the area shown in Figure 6d, at $m = 0$, 1, and 2 and the regression fits. After removing the mean, linear, and quadratic polynomials and annual and semi-annual sinusoids, the residual data are analyzed for the coseismic and postseismic changes. All five moment tensor components present significant coseismic and postseismic signature in the time series. Compared to the time series around the Maule earthquake, this area is affected less by systematic variations in gravity.

[66] The coseismic step and its error estimates for each of the localized coefficients were used for inversion of the moment tensor components at various depths. The solutions at 20 km are shown in Figure 21 along with other seismic solutions. The focal mechanism parameters were obtained for the primary and conjugate fault planes as also shown in Figure 21. All moment tensor components from GRACE at 20 km are in good agreement with seismic solutions. Once again, the fault plane solution with low dip angle yields nearly unity correlation between rake and strike, while it is not the case for the other fault plane. Therefore, we fix the strike a priori to obtain the double-couple solutions, and then test various strikes (Figure 22). Solutions featuring $M_0 = 450$–470×10^{20} N m (increasing with strike), $\delta = 14°$–$5°$ (decreasing with strike), λ changing linearly from 65° to 90° (increasing with strike), and $\phi_f = 175°$–$95°$ all fit the GRACE observations equally well, with VR ≥ 98%. The conjugate fault solution can be described with $M_0 = 450 \pm 20 \times 10^{20}$ N m, $\delta = 77° \pm 1°$, $\lambda = 95° \pm 3°$, when $\phi_f = 18° \pm 3°$.

[67] The solutions with the centroid in the upper mantle (depth greater than 24 km in PREM) indicated consistently poorer agreement with the GRACE observations, yielding VR ≈ 50%, compared to the ones within the upper and lower crust with VR > 90%. Therefore, we ruled out the solutions within the upper mantle and only show in Figure 23 the other solutions located within the crustal layers. The upper crustal solutions show dip angles of 7° and less and scalar moments of 380–600×10^{20} N m. The solutions within the lower crust indicate a dip ranging from 9° to 19° and M_0

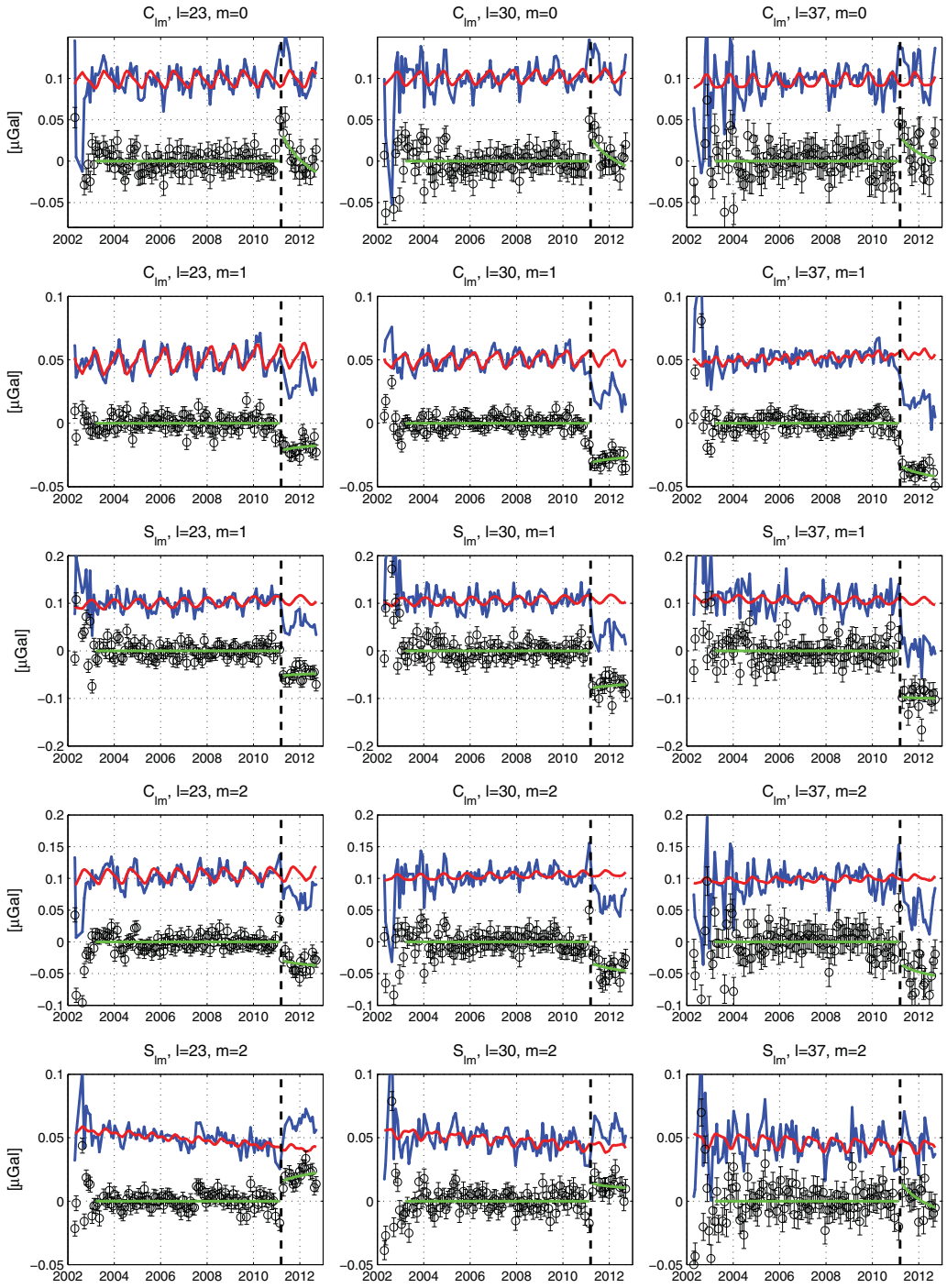

Figure 20. Same as Figure 7 for the 2011 Tohoku-Oki (Japan) earthquake. The GRACE coefficients were rotated in the coordinate system where the z axis locates at 38.5°N and 142.6°E. Higher noise in 2002 is due to the use of RL04 GRACE products. The quality of the product is improved with RL05 as shown in the rest of the years.

ranging 410 to 620×10^{20} N m, depending on the precise depth. In both cases, the shallower the depth in each layer, the smaller the dip and the larger the moment. When compared with other seismic and GPS-based solutions including long-period CMT and the moment-weighted CMT from various finite fault models [*Shao et al.*, 2011; *Simons et al.*, 2011; *Hayes*, 2011; *Ammon et al.*, 2011], only the GRACE solutions within the lower crust are consistent with those alternative solutions in moment and dip, as well as depth (except for the USGS CMT in depth).

[68] The coseismic gravity change (at a spatial resolution of 500 km), computed from the GRACE solution for a depth of 20 km, is shown in Figure 24a. It locates the primary negative anomaly in the back-arc region and the secondary positive anomaly (with one third the amplitude of the primary anomaly) near the trench. The alternative GRACE solutions

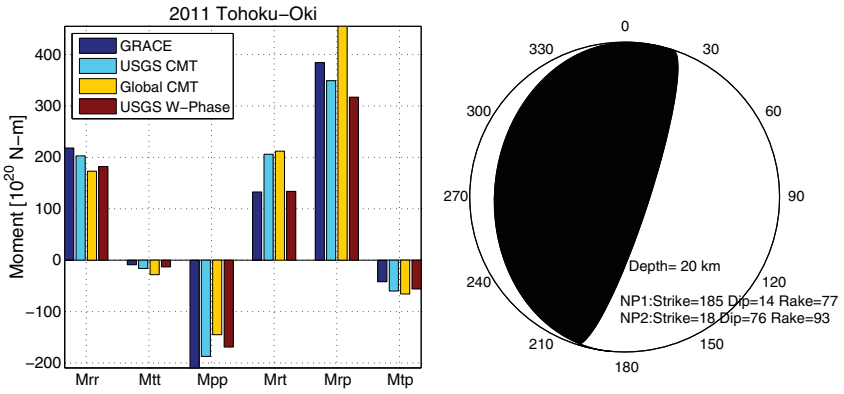

Figure 21. Same as Figure 8 for the 2011 Tohoku-Oki (Japan) earthquake.

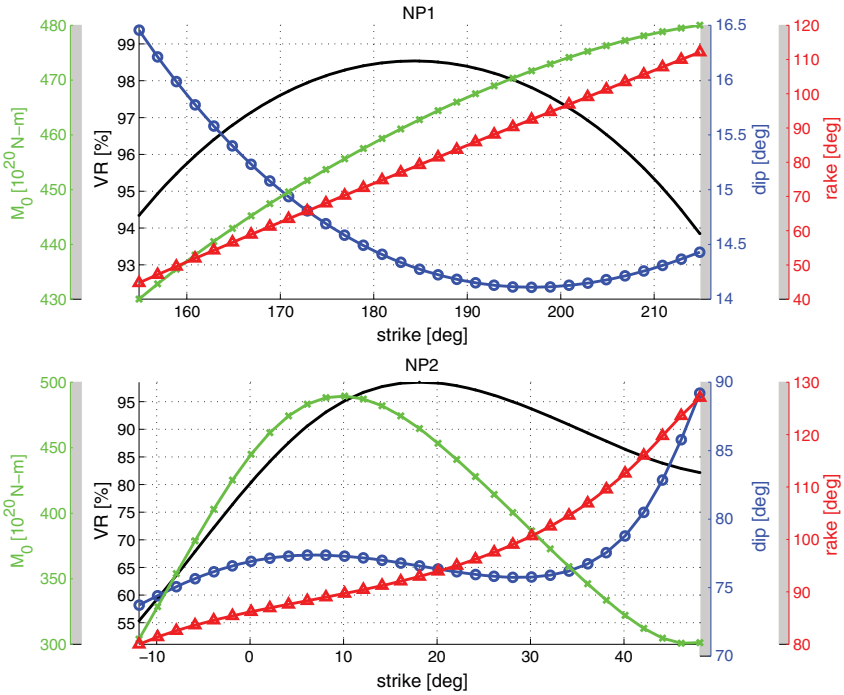

Figure 22. Same as Figure 10 for the 2011 Tohoku-Oki (Japan) earthquake. The depth was fixed at 20 km for all cases. The solutions with strike ranging from 175° to 195° are acceptable with VR ≥ 0.98 for the primary fault plane and the ones with strike from 15° to 23° are acceptable for the secondary fault plane.

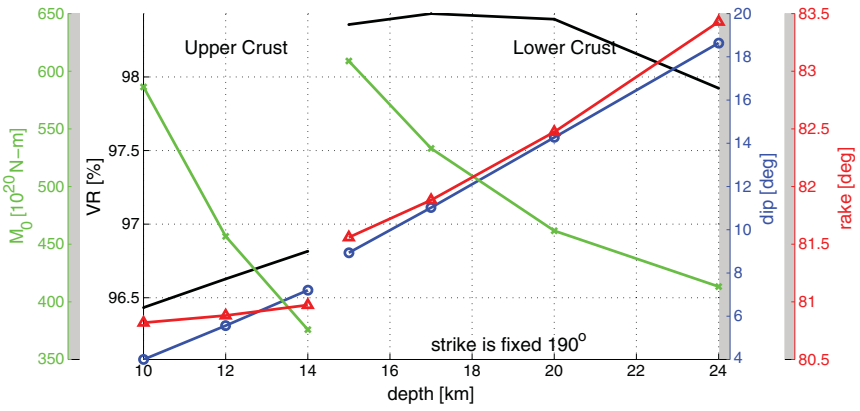

Figure 23. Same as Figure 11 for the 2011 Tohoku-Oki (Japan) earthquake. The strike was fixed at 190° for all cases.

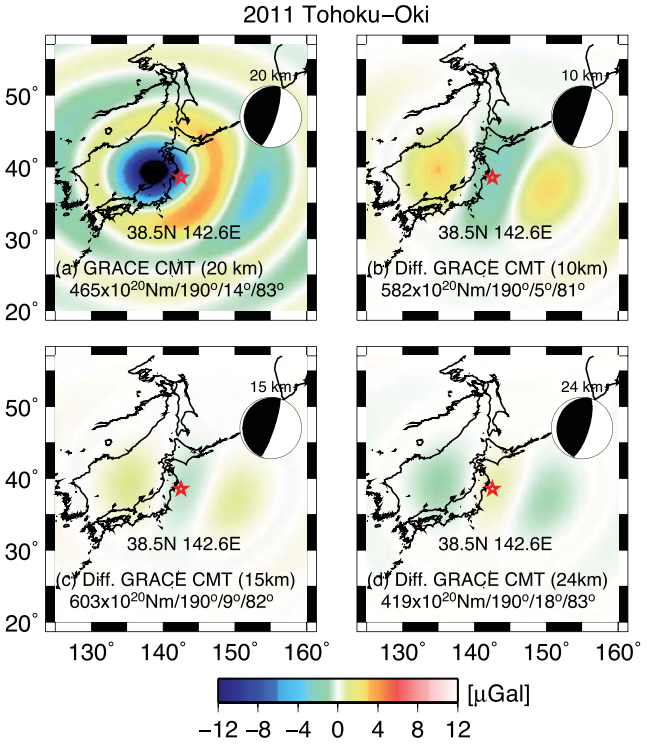

Figure 24. Same as Figure 12 for the 2011 Tohoku-Oki (Japan) earthquake. The location of the centroid is 38.5°N and 142.6°E.

at 10 (middle of the upper crust), 15 (upper bound of the lower crust), and 24 km (lower bound of the lower crust) are represented on Figures 24b–24d as deviations from the field of Figure 24a. They all remain within 1–2 μGal of the solution at 20 km.

6.5. 2012 Indian Ocean Strike-Slip Earthquake

[69] We examined the same GRACE coefficients for the same period but localized around the area where a sequence of great earthquakes ruptured in the Indian Ocean off Northern Sumatra on 11 April 2012 (Figure 6e). Figure 25 shows the time series from 2006 to September 2012. It was found that the long-term trend particularly evident in the dipolar coefficients, $C_{l,1}$ and $S_{l,1}$, is primarily due to the on-going viscoelastic deformation after the 2004 Sumatra-Andaman earthquake (e.g., numerical modeling such as in *Han et al*. [2008]). Unlike the previous earthquakes, the dipolar coefficients (for $M_{r\theta}$ and $M_{r\phi}$) do not show any significant coseismic change, while the quadratic coefficients such as $M_{\theta\phi}$ and $(M_{\theta\theta} - M_{\phi\phi})$ present a significant coseismic signature, albeit the latter component being noisier.

[70] The GRACE moment tensor estimates at depth 30 km were presented with other seismic solutions of the $M_w = 8.6$ main rupture on 11 April in Figure 26. It is clear that the GRACE estimates, indicating a composite of the ruptures, are substantially larger than seismic CMT solutions. The $M_{\theta\phi}$ estimate indicates a moment twice as large as derived from conventional seismic solutions. The initial focal mechanism is also computed and shown in Figure 26. The correlation matrix for the double-couple parameters does not show any strong coupling, for either fault plane, as shown in Figure 27. This is due to the large dip angle of both fault planes.

[71] Therefore, we inverted four double-couple parameters simultaneously from the moment tensor and its covariance estimates. Figure 28 shows these solutions for the primary and secondary fault planes at various depths from 10 to 50 km. All of them fit the GRACE data equally well, with VR ≥ 0.95. For the primary fault plane, $M_0 = 165–210 \times 10^{20}$ N m (decreasing with depth), $\delta = 78°–88°$ (increasing with depth), $\lambda = 183°–190°$ (decreasing with depth), and ϕ_f is more or less constant at 111°–113°, as depth changes from 10 to 50 km. For the secondary fault plane, within the same depth range, M_0 and δ are similar as for the first fault plane, while λ varies from −2° to −14° (decreasing with depth) and ϕ_f is more or less constant at 19°–22°.

[72] These double-couple solutions are relatively consistent regardless of depth, which is distinctly different from the previous thrust events. It can be explained as follows: The gravity change due to a strike-slip earthquake is characterized mostly by the quadratic gravity coefficients such as $C_{l,2}$ and $S_{l,2}$. Those coefficients are excited through the function K_2 in *Kanamori and Cipar* [1974]. As we extensively examined in Section 3, this function is nearly independent of depth at the range we considered in this study. These GRACE solutions are consistent with, or slightly larger than, the cumulative moment release during the first 2 h after the main rupture (139×10^{20} N m [*Yue, et al*., 2012]) combined with that of the aftershock (40×10^{20} N m [*Duputel et al*., 2012]).

[73] The coseismic gravity change (at a spatial resolution of 500 km) computed from the GRACE solution at a depth of 30 km (WNW-ESE plane) is shown in Figure 29a. It locates the primary quadrupolar anomaly at the epicenter. Although the free-air anomaly (surface and interior deformation) is shown in the figure, the Bouguer gravity anomaly (interior deformation) is very similar since the surface vertical deformation is small, as can be expected from Figure 3c. It indicates that the gravity anomaly from this earthquake is mostly from the interior process of compression (yielding positive gravity) and dilatation (yielding negative gravity). The alternative GRACE solutions at 30 km (a conjugate NNE-SSW plane), 10 km (WNW-ESE plane), and 50 km (WNW-ESE plane) are shown on Figures 29b–29d as deviations from the field of Figure 29a, respectively. The differences among them remain less than 1 μGal, meaning that all these double-couple solutions explain the GRACE gravity change equally well.

7. Summary and Discussion

[74] By analogy with the representation of seismic waves using normal mode summation, we obtained an analytic form for the coseismic gravitational potential changes induced by a point-source double-couple on the basis of the gravitational potential component of the elastogravitational normal mode eigenfunctions. A double-couple source excites isotropic, dipolar, and quadrupolar patterns of gravitational change that are expressed in terms of spherical harmonics (centered at the epicenter) in orders 0, 1, and 2, respectively. Each spherical harmonic coefficient is related to the moment tensor components of M_{rr}, $M_{r\theta}$, $M_{r\phi}$, $M_{\theta\theta} - M_{\phi\phi}$, and $M_{\theta\phi}$, in a simple linear manner.

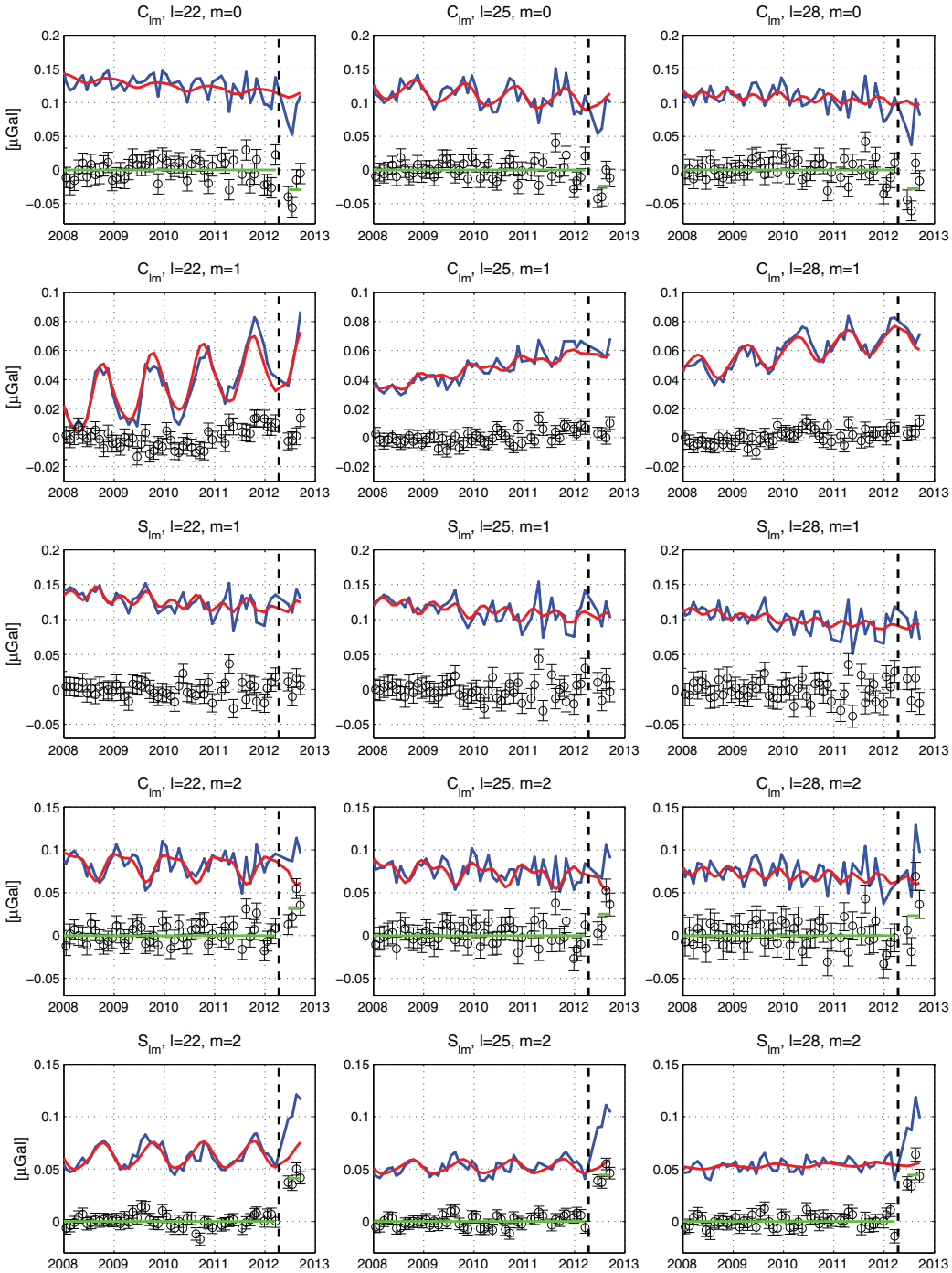

Figure 25. Same as Figure 7 for the 2012 Indian Ocean earthquake. The GRACE coefficients were rotated in the coordinate system where the z axis locates at 3.8°N and 101.0°E. The time series was drawn to start from 2006 to highlight 4 months of the GRACE observations after the rupture.

[75] Theoretical computations of the gravitational potential Green's functions $F_m(d_s)$ for shallow sources within layered Earth models yield the following results:

[76] 1. The fault depth (related to rigidity and bulk modulus) is critical to characterizing the spatial pattern and amplitude of the coseismic gravity perturbation, mostly through the isotropic component. For example, isotropic gravity responses from sources within the crustal layers and the upper mantle layer can be opposite in sign. In contrast, the quadrupolar ("strike-slip") function is independent of depth.

[77] 2. The interior deformation (density change) is more sensitive to the source depth and is larger than the surface deformation (Bouguer effect) for the shallower sources ($d_s < 20$ km).

[78] 3. For shallow thrust sources located in the upper crust, large-scale gravity data constrain only $M_0 \sin 2\delta$.

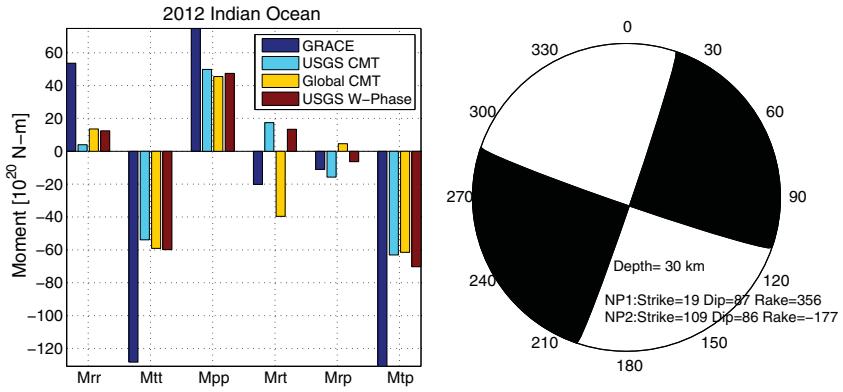

Figure 26. Same as Figure 8 for the 2012 Indian Ocean earthquake. Note that GRACE indicates a cumulative moment release from all events while various CMT solutions involve only the major event.

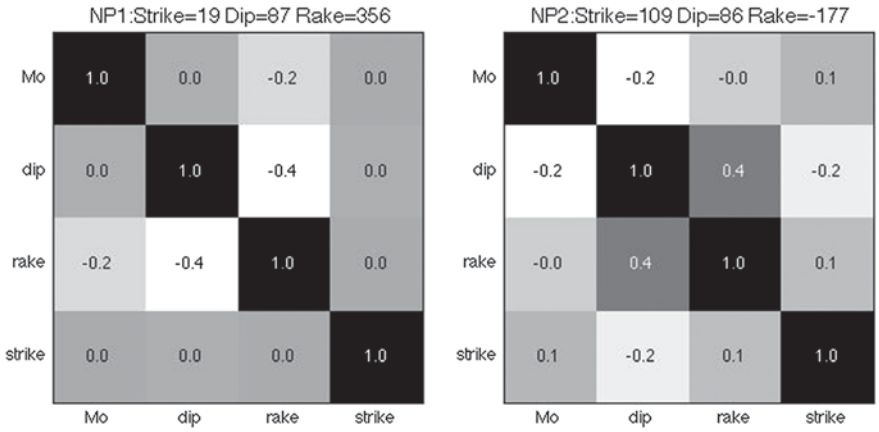

Figure 27. Same as Figure 9 for the 2012 Indian Ocean earthquake. Unlike the previous thrust events characterized by a shallow-dipping fault plane, there is no tight coupling among the double-couple parameters for both fault planes.

[79] 4. For low-dip thrust events, strike and rake are tightly coupled in a manner such that only their difference is constrained.

[80] All of these indicate that there might be trade-offs among the source parameters: scalar moment and dip with fault depth and strike and rake when dip is small.

[81] We developed an inversion method to estimate the fault parameters from global gravitational potential observations expressed as spherical harmonic coefficients, and applied it to the 2004 Sumatra-Andaman, 2010 Maule (Chile), 2011 Tohoku-Oki (Japan), and 2012 Indian Ocean earthquakes. A significant change in certain gravity coefficients related to $M_{r\theta}$ was also observed after the 2007 Bengkulu earthquake. For the thrust events, we found that centroid solutions within the upper and lower crust ($d_s < 25$ km) give considerably better fits to the GRACE data than the deeper ones do located within the upper mantle ($d_s > 25$ km). We interpret this result as due to an increase in bulk modulus (incompressibility) with depth responsible for the discordance in the resulting synthetics, as also found by *Cambiotti et al.* [2011]. In addition, crustal solutions (both upper and lower) yield more robust values of the parameter $\mu_s^{-1} M_0 \sin 2\delta$, where μ_s is the source rigidity, and thus of $\Delta u \sin 2\delta$ (where Δu is the seismic slip). Note that the latter is directly representative of the vertical component of slip in the limit angles δ for which $\cos\delta$ is stationary. Other seismic and geodetic solutions are consistent with the GRACE solutions within the lower crust. For the strike-slip events in 2012, the double-couple solutions present no significant depth-dependency and no trade-off among the fault parameters.

[82] In terms of spatial patterns of coseismic gravity changes, the GRACE observations consistently found primary negative gravity anomalies in the back-arc region and smaller positive anomalies offshore, for the three thrust events in 2004, 2010, and 2011. The negative anomaly originates mostly from the isotropic term expressing the influence of dilatation through the excitation function K_0 of *Kanamori and Cipar* [1974]. The deeper sources, located within the upper mantle with larger bulk and rigidity moduli than in the crust, cannot reproduce the larger negative gravity changes. In this respect, the satellite gravity observations from the megathrust events can be interpreted as expressing large-scale interior deformation associated with density changes (dilatation) inside the crustal layers. From the strike-slip event in 2012, the gravity change is, again, mostly from the interior process since the gravity effect from the vertical deformation at the crust-ocean interface is an order of magnitude smaller. The quadrupolar gravity pattern,

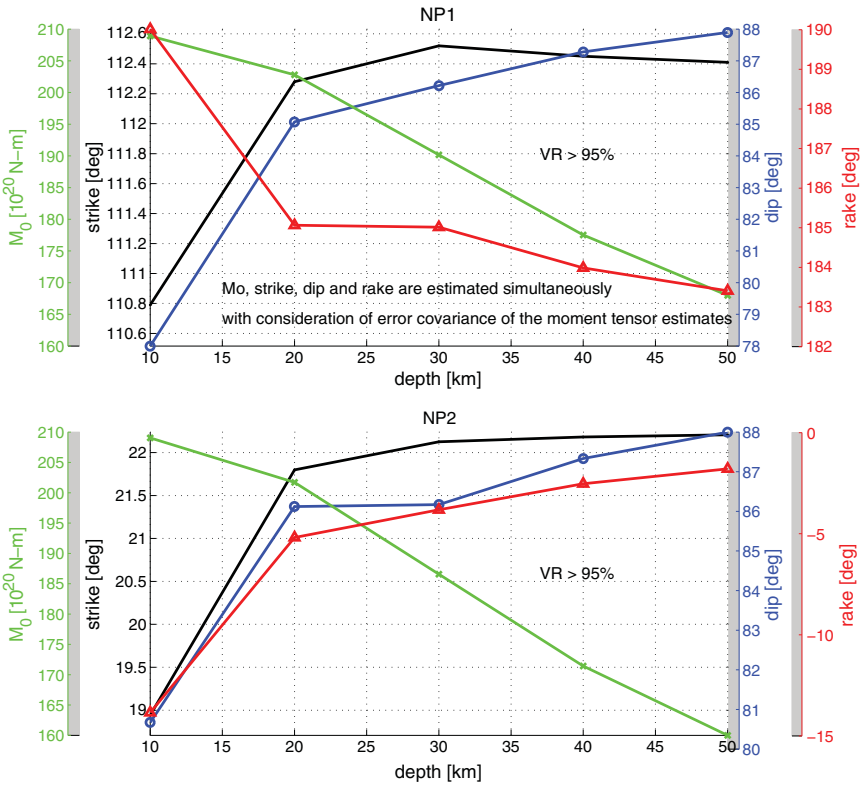

Figure 28. Same as Figure 11 for the 2012 Indian Ocean earthquake. In this earthquake, the simultaneous solutions of the double-couple parameters were obtained at various depths for both fault planes (due to no tight coupling among the parameters). All the solutions produce VR $\geq$ 0.95. A distinct difference from the previous thrust events is that the double-couple solutions of this strike-slip earthquake are relatively consistent regardless of depths. The scalar moment estimate from GRACE is consistent with the cumulative moment release from a series of the main ruptures and aftershocks.

being positive in ENE and WSW quadrants and negative in NNW and SSE quadrants, indicates compression and dilatation, respectively, radially inside the Earth.

[83] Our work also offers the possibility of investigating the presence of any ultraslow components in the spectrum of the seismic source. The largest ever earthquake recorded, the 1960 Chilean event was documented by *Kanamori and Cipar* [1974], *Kanamori and Anderson* [1975] and *Cifuentes and Silver* [1989] to include a slow precursor, which started 15 min before the high-frequency rupture, and may have had a comparable moment. Similarly, a number of studies of the 2004 Sumatra earthquake (including the modeling of its normal modes) have shown that its very-long period moment, 1.15×10^{23} N m, was more than 2.5 times greater than that derived from the standard GCMT algorithm, indicating an element of slowness also expressed in other characteristics of its source [*Stein and Okal*, 2005; *Tsai et al*., 2005; *Choy and Boatwright*, 2007]. Preliminary evidence also suggests that the 1964 Alaska earthquake, and possibly the Rat Island earthquake of 1965, may have featured a similar component of source slowness [*Nettles et al*., 2005]. By contrast, the normal modes of the 2010 Chilean and 2011 Tohoku events do not reveal any such slowness [*Okal et al*., 2012; *Okal*, 2012].

[84] Because the inversion of GRACE L2 data uses successive orbits for a month, the seismic moments resolved in the present study represent averages over a time window much longer than accessible from seismic data. The latter are limited in principle by the period of the Earth's gravest mode, ${}_0S_2$ (3232 s), and in practice most classical CMT inversions are carried at periods not exceeding 300 s. Consequently, the comparison between our results and classical seismological ones can shed some light on the behavior of the source on time scales transgressing the seismic spectrum: a significant disparity between a GRACE moment and a (seismic) CMT solution would be a proxy for the existence of a slow source component releasing moment at frequencies below that of ${}_0S_2$, while obviously it could not resolve the details of such a component (e.g., whether it was precursory, coseismic or took place 10 days after the main shock).

[85] 1. For the 2004 Sumatra-Andaman earthquake, the composite GRACE solution consisting of four sources elongated along strike yields a composite moment of 1.2×10^{23} N m with a dip of 10°, in excellent agreement with the value of 1.2×10^{23} N m obtained at ultralong seismic periods by *Tsai et al*. [2005] and *Okal and Stein* [2009], and about 2.5 to 3 times greater than the classical GCMT solution. We conclude that GRACE confirms the slow components occasionally documented at frequencies lower than those of CMT inversions, but fails to unearth even slower ones, with characteristic times of hours to days, whose existence could not have been a priori excluded.

[86] 2. For the 2010 Maule, Chile earthquake, our solutions range from 2.0 to 2.7×10^{22} N m for dips between 12° and 24°, and centroid depths between 15 and 24 km.

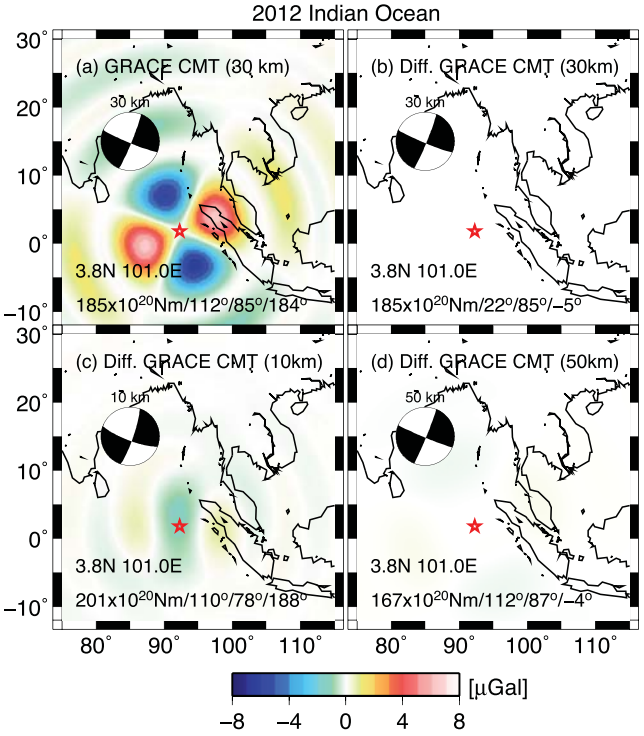

Figure 29. Same as Figure 12 for the 2012 Indian Ocean earthquake. The location of the centroid is 3.8°N and 101.0°E. Figure 29 a stands for the WNW-ESE fault plane while Figure 29b the NNE-SSW plane at the same depth of 30 km. Note that the surface gravity is not significantly different even with a wide range of variation in centroid depth.

These numbers compare favorably with finite fault models such as *Lay et al.*'s [2010] ($M_0 = 2.1 \times 10^{22}$ N m), and are only about 20% greater than the GCMT solution.

[87] 3. In the case of the 2011 Tohoku-Oki earthquake, scalar moments estimated from GRACE data range from 4.1 to 6.1×10^{22} N m, with dips between 9° and 19° and depths between 15 and 24 km. This is in excellent agreement with the published GCMT value (5.3×10^{22} N m) and supports *Okal*'s [2012] conclusion that the earthquake does not feature anomalous source slowness.

[88] 4. For the 2012 Indian Ocean strike-slip earthquakes, GRACE estimates the scalar moment at 1.9×10^{22} N m at a depth of 30 km, 60% larger than the combined GCMT values for the mainshock and aftershock (0.9×10^{22} N m and 0.3×10^{22} N m respectively), but comparing favorably with the total moment of 1.4×10^{22} N m of the finite fault solution of the main shock sequence by *Yue et al.* [2012] combined with the estimate of 0.3×10^{22} N m for the aftershock [*Duputel et al.*, 2012].

[89] 5. The detection of the 2007 Bengkulu earthquake ($M_0 = 50 \times 10^{20}$ N m; $M_w = 8.5$) may demonstrate the lower bound for the use of GRACE gravity data to resolve earthquake deformation. This was feasible due to the highest sensitivity of GRACE data to gravity change in N-S direction, where the spatial resolution could improve 400–500 km to as little as 200–300 km.

[90] In this work, we attempted to characterize five great earthquakes in terms of a centroid (point) representation, although the laterally and vertically distributed moments or slips with a finite dimension of fault would be more suitable for such large earthquakes. Our quantification of the centroid sources from gravity observations compares, in general, favorably with other seismic centroid solutions. When jointly analyzed with other terrestrial data (like GPS and seismic records), GRACE gravity data will provide seldom-observed, broad-scale constraints on the spatial distribution of slip.

[91] The gradual postseismic changes over a time frame of several years observed in most cases should not be overlooked. Continuous observations of gravitational potential changes will be useful to document the rheological response of the Earth to great earthquakes and to advance our understanding of post-earthquake stress and strain redistribution. These data could provide, for example, an insight into bulk behavior: time-dependent (inelastic) bulk modulus [*Rundle*, 1978; *Rundle and Smith*, 1982] versus no significant bulk relaxation [*Cohen*, 1980a, 1980b; *Ivins and Sammis*, 1996; *Pollitz*, 1997]. These could be indispensable for understanding the large-scale behavior of the Earth's shallow material, and eventually for earthquake hazard assessment and mitigation applications. Finally, the future GRACE follow-on mission equipped with enhanced instrumentation [*Watkins*, 2011] may allow us to exploit gravitational potential data in the analysis of smaller, and thus more frequent seismic events than the ones studied here. The transient gravitational perturbations available from L1B orbit perturbation data could deliver additional understanding at the seismic frequencies.

Appendix A: On the Behavior of Isotropic Gravity Response From Shallow Sources

[92] In order to investigate the isotropic gravity response function $F_0(d_s)$, we examine the excitation function ${}_nK_{0,l}$ given in *Kanamori and Cipar* [1974] using the eigenfunction components defined by *Alterman et al.* [1959]. This can be rewritten by introducing the dilatation component as (we specify here the degree l and overtone n, explicitly):

$$ {}_nK_{0,l}(d_s) = \frac{2l+1}{4\pi {}_n\sigma_l^2 [I_1 + l(l+1)I_2]} \left\{ {}_nX_l(d_s) - 3\,{}_n\dot{y}_{1,l}(d_s) \right\}, \quad \text{(A1)} $$

where ${}_n\sigma_l$ is the eigenfrequency; ${}_nX_l$ is the dilatation eigenfunction that can be written as ${}_nX_l = {}_n\dot{y}_{1,l} + \frac{2}{r}\,{}_ny_{1,l} - \frac{l(l+1)}{r}\,{}_ny_{3,l}$, and ${}_n\dot{y}_{1,l}$ is the radial derivative of ${}_ny_{1,l}$: ${}_n\dot{y}_{1,l} = \frac{-2\bar{\lambda}}{(\bar{\lambda}+2\mu)r}\,{}_ny_{1,l} + \frac{1}{(\bar{\lambda}+2\mu)}\,{}_ny_{2,l} + \frac{\bar{\lambda}l(l+1)}{(\bar{\lambda}+2\mu)r}\,{}_ny_{3,l}$ with the Lamé constants $\bar{\lambda}$ and μ (we use the notation $\bar{\lambda}$ to distinguish it from the rake angle λ); y_3 is the horizontal displacement component of the eigenfunction; I_1 and I_2 are energy integrals defined in *Kanamori and Cipar* [1974]. These functions need to be evaluated at the source depth d_s to compute the change in gravitational potential at the surface. The traction component of the eigenfunction, y_2, must vanish at the surface and remains small at shallow depths. We can thus approximate ${}_ny_{2,l} = \bar{\lambda}\,{}_nX_l + 2\mu\,{}_n\dot{y}_{1,l} \approx 0$, and obtain ${}_n\dot{y}_{1,l} \approx -\frac{\bar{\lambda}}{2\mu}\,{}_nX_l$. In turn, the following approximation will hold for shallow sources:

$$ {}_nK_{0,l}(d_s) \approx \frac{(2l+1)}{4\pi {}_n\sigma_l^2 [I_1 + l(l+1)I_2]} \left\{ \frac{3\bar{\lambda}+2\mu}{2\mu} \right\} {}_nX_l(d_s). \quad \text{(A2)} $$

[93] Alternatively and introducing Poisson's ratio $v = \frac{\bar{\lambda}}{2(\bar{\lambda}+\mu)}$,

$$ {}_nK_{0,l}(d_s) \approx \frac{(2l+1)}{4\pi_n\sigma_l^2[I_1 + l(l+1)I_2]} \left\{\frac{1+v}{1-2v}\right\} {}_nX_l(d_s). \qquad \text{(A3)} $$

Note in particular that under this approximation, ${}_nK_{0,l}$ becomes proportional to the excitation coefficient ${}_nN_{0,l}$ for an explosive source [*Okal*, 1978]:

$$ {}_nK_{0,l}{}^n \approx -\frac{3\lambda+2\mu}{2\mu} {}_nN_{0,l} = -\frac{1+v}{1-2v} {}_nN_{0,l}. \qquad \text{(A4)} $$

[94] In the PREM model, $(1+v)/(1-2v)$ varies only from 2.6 to 2.9 within the upper and lower crust and the upper mantle. As a result, (A4) implies that dilatation in the source region will directly influence the isotropic gravity response function $F_0(d_s)$.

[95] **Acknowledgments.** This work was supported by the NASA Earth Surface and Interior program and the GRACE project. We thank DLR for providing the GRACE telemetry data and JPL and CSR for producing the high-quality level 1B and level 2 products. We thank Fred Pollitz, Richard Gross, Erik Ivins, Caroline de Linage, Luis Rivera, and Frederik Simons for helpful discussions. We thank two anonymous reviewers and an associate editor for the constructive comments to improve our original manuscript.

References

Aki, K., and P. Richards (1980), Quantitative Seismology: Theory and Methods, Freeman Co., New York.

Alterman, Z., H. Jarosch, C. Pekeris (1959), Oscillations of the Earth, *Proc. Roy. Soc. London, A*, *252*: 80–95.

Ammon, C. J., T. Lay, H. Kanamori, and M. Cleveland (2011), A rupture model of the 2011 off the Pacific coast of Tohoku earthquake, *Earth Planets Space*, *63*, 693–696.

Bassin, C., G. Laske, and G. Masters (2000), The current limits of resolution for surface wave tomography in North America, *Eos Trans. AGU*, *81*, F897.

Bettadpur, S. (2012), Insights into the Earth system mass variability from CSR-RL05 GRACE gravity fields, *Geophys. Res. Abstr.*, Vol. *14*, EGU2012-6409, EGU General Assembly held 22-27 April 2012 in Vienna, Austria., p. 6409.

Borrero, J. C., R. Weiss, E. A. Okal, R. Hidayat, Suranto, D. Arcas, and V. V. Titov (2009), The tsunami of 12 September 2007, Bengkulu Province, Sumatra, Indonesia: Post-tsunami survey and numerical modeling, *Geophys. J. Intl.*, *178*, 180–194.

Brink, D.M., and G.R. Satchler (1968), Angular Momentum, Clarendon Press, Oxford.

Broerse, D. B. T., L. L. A. Vermeersen, R. E. M. Riva, and W. van der Wal (2011), Ocean contribution to co-seismic crustal deformation and geoid anomalies: Application to the 2004 December 26 Sumatran-Andaman earthquake, *Earth Planet. Sci. Lett.*, *305*, 341–349, doi:10.1016/j.epsl.2011.03.011.

Bromwich, T.J.I.'A. (1898), On the influence of gravity on elastic waves, and, in particular, on the vibrations of an elastic globe, *Proc. London Mat. Soc.*, *30*, 98−120

Cambiotti, G., A. Bordoni, R. Sabadini, and L. Colli (2011), GRACE gravity data help constraining seismic models of the 2004 Sumatran earthquake, *J. Geophys. Res.*, *116*, B10403, doi:10.1029/2010JB007848.

Cambiotti, G., and R. Sabadini (2012), A source model for the great 2011 Tohoku earthquake (M_w = 9.1) from inversion of GRACE gravity data, *Earth Planet. Sci. Lett.*, *335–336*, 72–79.

Cifuentes, I.L., and P.G. Silver (1989), Low-frequency source characteristics of the great 1960 Chilean earthquake, *J. Geophys. Res.*, *94*, 643−663.

Chao, B.F. and R.S. Gross (1987), Changes in the Earth's rotation and low-degree gravitational field induced by earthquakes. *Geophys. J. R. Astron. Soc. 91*, 569–596.

Chinnery, M.A. (1975), The static deformation of an Earth with a fluid core: A physical approach, *Geophys. J. Roy. Astr. Soc.*, *42*, 461−475.

Chlieh, M., et al. (2007), Coseismic slip and afterslip of the great Mw 9.15 Sumatra-Andaman earthquake of 2004, *Bull. Seismol. Soc. Amer.*, *97*, S152-S173.

Choy, G.L., and J. Boatwright (2007), The energy radiated by the 26 December 2004 Sumatra-Andaman earthquake estimated from 10-minute P-wave windows, Bull, *Seismol. Soc. Amer.*, *97*, S18–S24.

Cohen, S. C. (1980a), Postseismic viscoelastic surface deformation and stress: 1. Theoretical considerations, displacement, and strain calculations, *J. Geophys. Res.*, *85*(B6), 3131–3150, doi:10.1029/JB085iB06p03131.

Cohen, S. C. (1980b), Postseismic viscoelastic deformation and stress: 2. Stress theory and computation; dependence of displacement, strain, and stress on fault parameters, *J. Geophys. Res.*, *85*(B6), 3151–3158, doi:10.1029/JB085iB06p03151.

De Linage C., L. Rivera, J. Hinderer, J.P. Boy, Y. Rogister, S. Lambotte, and R. Biancale (2009), Separation of coseismic and postseismic gravity changes for the 2004 Sumatra-Andaman earthquake from 4.6 yr of GRACE observations and modelling of the coseismic change by normal-modes summation, *Geophy. J. Int.*, *176*, 695–714.

Duputel, Z., H. Kanamori, V. C. Tsai, L. Rivera, L. Meng, J-P. Ampuero, and J. Stock (2012), The 2012 Sumatra great earthquake sequence, *Earth and Planetary Science Letters*, *351–352*, 247–257.

Dziewonski, A. M., and D. L. Anderson (1981), Preliminary Reference Earth Model. *Phys. Earth Planet. Inter. 25*, 297–356.

Gilbert, J.F. (1970), Excitation of the normal modes of the Earth by earthquake sources, *Geophys. J. Roy. Astr. Soc.*, *22*, 223−226.

Gilbert, F. and G. Backus (1968), Elastic-gravitational vibrations of a radially stratified sphere, in Dynamics of Stratified Solids, edited by G. Herrmann, p. 82–95, Am. Soc. Mech. Eng., New York.

Han, S.-C. C. K. Shum, C. Jekili, C.-Y. Kuo, and C. Wilson (2005), Non-isotropic filtering of GRACE temporal gravity for geophysical signal enhancement, *Geophys. J. Int.*, *163*, 18–25.

Han, S. C., and P. Ditmar (2008), Localized spectral analysis of global satellite gravity fields for recovering time–variable mass redistributions, *J. Geod.*, *82*, 423–430, doi:10.1007/s00190-007-0194-5.

Han, S.-C., and F. J. Simons (2008), Spatiospectral localization of global geopotential fields from the Gravity Recovery and Climate Experiment (GRACE) reveals the coseismic gravity change owing to the 2004 Sumatra-Andaman earthquake, *J. Geophys. Res.*, *113*, B01405, doi:10.1029/2007JB004927.

Han, S.-C., C.K. Shum, M. Bevis, C. Ji, and C. Kuo (2006), Crustal dilatation observed by GRACE after the 2004 Sumatra-Andaman earthquake, *Science*, *313*, 658–662.

Han, S.-C., J. Sauber, S. Luthcke, C. Ji, and F. Pollitz (2008), Implications of postseismic gravity change following the great 2004 Sumatra-Andaman earthquake from the regional harmonic analysis of GRACE intersatellite tracking data, *J. Geophys. Res.*, *113*, B11413, doi:10.1029/2008JB005705.

Han, S.-C., J. Sauber, and S. Luthcke (2010), Regional gravity decrease after the 2010 Maule (Chile) earthquake indicates large-scale mass redistribution, *Geophys. Res. Lett.*, *37*, L23307, doi:10.1029/2010GL045449.

Han, S.-C., J. Sauber, and R. Riva (2011), Contribution of satellite gravimetry to understanding seismic source processes of the 2011 Tohoku-Oki earthquake, *Geophys. Res. Lett.*, *38*, L24312, doi:10.1029/2011GL049975.

Hayes, G. P. (2011), Rapid source characterization of the Mw 9.0 off the Pacific coast of Tohoku Earthquake. *Earth Planets Space*, *63*, 529–534.

Heki, K., and K. Matsuo (2010), Coseismic gravity changes of the 2010 earthquake in central Chile from satellite gravimetry, *Geophys. Res. Lett.*, *37*, L24306, doi:10.1029/2010GL045335.

Hoechner, A., S. V. Sobolev, I. Einarsson, and R. Wang (2011), Investigation on afterslip and steady state and transient rheology based on postseismic deformation and geoid change caused by the Sumatra 2004 earthquake, *Geochem. Geophys. Geosyst.*, *12*, Q07010, doi:10.1029/2010GC003450.

Ivins, E.R., and C.G. Sammis (1996), Transient creep of a composite lower crust: 1. Constitutive theory, *J. Geophys. Res.*, *101*, 27,981–28,004.

Jeffreys, H. (1976), The Earth: Its Origin, History and Physical Constitution, 6th ed., 574 pp., Cambridge Univ. Press, New York.

Kanamori, H., and D.L. Anderson (1975), Amplitude of the Earth's free oscillations and long-period characteristics of the earthquake source, *J. Geophys. Res.*, *80*, 1075−1078.

Kanamori, H. and J.J. Cipar (1974), Focal process of the great Chilean earthquake, May 22, 1960, *Phys. Earth Planet. Inter.*, *9*, 128–136.

Kanamori, H. and Given, J.W. (1981), Use of long-period surface waves for rapid determination of earthquake source parameters, *Phys. Earth Planet. Int.*, *27*, 8–31.

Lamb, H. (1882), On the vibrations of an elastic sphere, *Proc. London Mat. Soc.*, *19*, 189−212.

Lay, T., J. Ammon, H. Kanamori, K. D. Koper, O. Surfi, and A. R. Hutko (2010), Teleseismic inversion for rupture process of the 27 February 2010 Chile (M_w 8.8) earthquake, *Geophys. Res. Lett.*, *37*, L13301, doi:10.1029/2010GL043379.

Longman, I. M. (1962), A Green's function for determining the deformation of the Earth under surface mass loads: 1. Theory, *J. Geophys. Res.*, *67*, 845−850.

Longman, I.M. (1963), A Green's function for determining the deformation of the Earth under surface mass loads: 2. Computations and numerical results, *J. Geophys. Res.*, *68*, 485−496.

Love, A.E.H. (1911), Some Problems of Geodynamics, Chap X, Cambridge University Press.

Matsuo, K., and K. Heki (2011), Coseismic gravity changes of the 2011 Tohoku-Oki earthquake from satellite gravimetry, *Geophys. Res. Lett.*, *38*, L00G12, doi:10.1029/2011GL049018.

Nettles, M., G. Ekström, A.M. Dziewonski, and N. Maternovskaya (2005), Source characteristics of the great Sumatra earthquake and its aftershocks, Eos, *Trans. Amer. Geophys. Un.*, *86*, (18), U43A-01 [abstract].

Ogawa, R., and K. Heki (2007), Slow postseismic recovery of geoid depression formed by the 2004 Sumatra-Andaman earthquake by mantle water diffusion, *Geophys. Res. Lett.*, *34*, L06313, doi:10.1029/2007GL029340.

Okal, E.A. (1978), A physical classification of the Earth's spheroidal modes, *J. Phys. Earth*, *26*, 75–103.

Okal, E.A. (2012), From 3-Hz P waves to ${}_0S_2$: No evidence of a slow component to the source of the 2011 Tohoku earthquake, *Pure Appl. Geophys.*, in press.

Okal, E.A., and S. Stein (2009), Observations of ultra-long period normal modes from the 2004 Sumatra-Andaman earthquake, *Phys. Earth Planet. Inter.*, *175*, 53−62.

Okal, E.A., S. Hongsresawat, and S. Stein (2012), Split mode evidence for no ultra-slow component to the source of the 2010 Maule, Chile earthquake, *Bull. Seismol. Soc. Amer.*, *102*, 391−397.

Okubo, S. (1992), Gravity and potential changes due to shear and tensile faults in a half-space, *J. Geophys. Res.*, *97*, 7137-7144.

Panet, I., F. Pollitz, V. Mikhailov, M. Diament, P. Banerjee, and K. Grijalva (2010), Upper mantle rheology from GRACE and GPS postseismic deformation after the 2004 Sumatra-Andaman earthquake, *Geochem. Geophys. Geosyst.*, *11*, Q06008, doi:10.1029/2009GC002905.

Pekeris, C. L., and H. Jarosch (1958), The free oscillations of the Earth, in *Contributions in Geophysics in Honor of Beno Gutenberg*, vol.1, pp. 171–192, edited by H. Benioff, M. Ewing, B. Howell, and F. Press, Pergamon., New York.

Piersanti, A., G. Spada, R. Sabadini, and M. Bonafede (1995), Global postseismic deformation, *Geophys. J. Int. 120*, 544-566.

Pollitz, F.F. (1992), Postseismic relaxation theory on the spherical Earth, *Bull. Seismol. Soc. Am.*, *82*, 422-453.

Pollitz, F. (1996), Coseismic deformation from earthquake faulting on a layered spherical Earth, *Geophys. J. Int.*, *125*, 1-14.

Pollitz, F. (1997), Gravity anomaly from faulting on a layered spherical earth with application to central Japan, *Phys. Earth Planet. Int.*, *99*, 259–271.

Pollitz, F., R. Bürgmann, P. Banerjee (2006), Postseismic relaxation following the great 2004 Sumatra-Andaman earthquake on a compressible self-gravitating Earth, *Geophys. J. Int.*, *167*, 397–420.

Pollitz, F. F, et al. (2011), Coseismic slip distribution of the February 27, 2010 Mw 8.8 Maule, Chile earthquake, *Geophys. Res. Lett.*, L09309, doi:10.1029/2011GL047065.

Rundle, J. B. (1978), Viscoelastic crustal deformation by finite quasi-static sources, *J. Geophys. Res.*, *83*(B12), 5937–5945, doi:10.1029/JB083iB12p05937.

Rundle, J. B., and A. T. Smith (1982), Comment on 'Interpretation of postseismic deformation with a viscoelastic relaxation model,' by J. Wahr and M. Wyss, *J. Geophys. Res.*, *87*(B2), 1079–1080, doi:10.1029/JB087iB02p01079.

Saito, M. (1967), Excitation of free oscillations and surface waves by a point source in a vertical heterogeneous Earth, *J. Geophys. Res.*, *72*, 3689–3699.

Sato, Y. (1950), Transformations of wave functions related to the transformations of coordinate systems, *Bull. Earthq. Res. Inst. Tokyo Univ.*, *28*, 175−217.

Shao, G., X. Li, C. Ji, T. Maeda (2011), Focal mechanism and slip history of 2011 Mw 9.1 off the Pacific coast of Tohoku Earthquake, constrained with teleseismic body and surface waves. *Earth Planets Space*, *63*, 559–564.

Simons, M., S. Solomon, and B. Hager (1997), Localization of gravity and topography: Constraints on the tectonics and mantle dynamics of Venus, *Geophys. J. Int.*, *131*, 24–44.

Simons, M., et al. (2011), The 2011 magnitude 9.0 Tohoku-Oki earthquake: Mosaicking the megathrust from seconds to centuries. *Science 332*, 1421.

Stein, S., and R.J. Geller (1977), Amplitudes of the Earth's split normal modes, *J. Phys. Earth*, *25*, 117−142.

Stein, S., and E.A. Okal (2005), Size and speed of the Sumatra earthquake, *Nature*, *434*, 581−582.

Smylie, D.E., and L. Mansinha (1971), The elasticity theory of dislocations in real Earth models and changes in the rotation of the Earth, *Geophys. J. Roy. Astr. Soc.*, *23*, 329−354.

Tapley, B., et al. (2005), GGM02–An improved Earth gravity field model from GRACE, *J. Geodesy*, *79*, 467-478.

Tsai, V. C., M. Nettles, G. Ekström, and A. M. Dziewonski (2005), Multiple CMT source analysis of the 2004 Sumatra earthquake, *Geophys. Res. Lett.*, *32*, L17304, doi:10.1029/2005GL023813.

Tsai, V. C., G. P. Hayes, and Z. Duputel (2011), Constraints on the long period moment dip tradeoff for the Tohoku earthquake, *Geophys. Res. Lett.*, *38*, L00G17, doi:10.1029/2011GL049129.

Turcotte, D. L., R. J. Willemann, W. F. Haxby, and J. Norberry (1981), Role of membrane stresses in the support of planetary topography, *J. Geophys. Res.*, *86*, 3951–3959.

Vermeersen, L.L.A., R. Sabadini, and G. Spada (1996), Compressible rotational deformation, *Geophys. J. Intl.*, *126*, 735−761.

Wang, L., C. K. Shum, F. J. Simons, B. Tapley, and C. Dai (2012), Coseismic and postseismic deformation of the 2011 Tohoku-Oki earthquake constrained by GRACE gravimetry, *Geophys. Res. Lett.*, *39*, L07301, doi:10.1029/2012GL051104.

Watkins, M. (2011), GRACE follow-on mission status. A paper presented at GRACE Science Team meeting, Austin, Tex, August 8-10.

Wieczorek, M. A., and F. J. Simons (2005), Localized spectral analysis on the sphere, *Geophys. J. Int.*, *162*, 655–675, doi:10.1111/j.1365-246X.2005.02687.x.

Yue, H., T. Lay, K. Koper (2012), En echelon and orthogonal fault ruptures of the 11 April 2012 great intraplate earthquakes, *Nature*, *490*, 245-250, doi:10.1038/nature11492.